

Electronic Thesis and Dissertation Repository

10-23-2020 2:00 PM

Improving the Transient Stability of the Virtual Synchronous Generator

Kourosh Gharouni Saffar, *The University of Western Ontario*

Supervisor: Firouz Badrkhani Ajaei, *The University of Western Ontario*

A thesis submitted in partial fulfillment of the requirements for the Master of Engineering Science degree in Electrical and Computer Engineering

© Kourosh Gharouni Saffar 2020

Follow this and additional works at: <https://ir.lib.uwo.ca/etd>

Recommended Citation

Gharouni Saffar, Kourosh, "Improving the Transient Stability of the Virtual Synchronous Generator" (2020). *Electronic Thesis and Dissertation Repository*. 7418.
<https://ir.lib.uwo.ca/etd/7418>

This Dissertation/Thesis is brought to you for free and open access by Scholarship@Western. It has been accepted for inclusion in Electronic Thesis and Dissertation Repository by an authorized administrator of Scholarship@Western. For more information, please contact wlsadmin@uwo.ca.

Abstract

The majority of the Distributed Energy Resources (DERs), i.e., Energy Storage Systems (ESSs) and Renewable Energy Systems (RESs), utilize inverters to convert the Direct Current (DC) power to the Alternating Current (AC) power needed by the majority of the consumers. Proliferation of the inverter-based DERs has caused significant changes in the operation of the modern electric power systems. Inverters lack the mechanical inertia that is inherent in the traditional power generators, i.e., rotating electrical machines. As a result, the emerging inverter-dominated power systems suffer from lower stability margins, excessive frequency deviations, and poor dynamic response to disturbances. This issue has adversely affected the integration of the highly advantageous inverter-based renewable energy systems in microgrids and active distribution systems. Appropriate inverter control can be used to emulate virtual inertia by imitating the behavior of traditional generation units. Based on this idea, the concept of virtual synchronous generator (VSG) has been proposed.

VSGs suffer from the transient stability issues that affect the operation of the Synchronous Generators (SGs). They can become unstable due to prolonged faults. Unlike the SGs that can handle significant over-current stress, VSGs have limited overcurrent capacity. The studies conducted in this research indicate that the current limiting strategy of the VSG significantly impacts its transient stability. The impacts of different inverter current limiting strategies on the performance of the VSG are investigated and the one that leads to the largest transient stability margin is identified. In addition, the impact of the VSG damping factor on the critical clearing time is investigated and specific conditions to maintain transient stability are devised. Based on the results of these studies, an adaptive damping control scheme is proposed to enhance the transient stability of the VSG.

The acceptable performance of the proposed control strategies is verified through numerous fault studies conducted on a realistic study system in the PSCAD/EMTDC software environment. The study results indicate that the proposed adaptive damping control strategy: (i) is simple and easy to implement, (ii) does not require communication between distributed energy resources, (iii) significantly improves the dynamic response of the VSG to disturbances and the VSG transient stability, and (iv) enables the VSG to ride through prolonged faults without becoming unstable.

Keywords: Inertia emulation, virtual synchronous machine, transient stability, fault ride through, critical clearing time.

Summary for Lay Audience

The penetration of renewable energy sources into power system has been rising in recent years. Proliferation of these technologies has caused significant changes in the design and operating principles of the modern electric power systems. Due to the physical characteristics of these resources and the fact that they are typically interfaced to the power grid by power electronics converters, i.e., inverters, their interaction with the grid is substantially different from those of the traditional power generation plants. While the rotating parts in the traditional power generators inherently provide inertia to the system, inverter-interfaced renewable energy systems lack the mechanical inertia. This lack of inertia can cause instability issues. This thesis identifies the best technical practices and develops innovative solutions to improve the stability of the modernized grid in presence of renewable energy sources.

To my family, who have supported me each step of the way.

Acknowledgments

I would like to first and foremost express my sincerest gratitude to my supervisor, Dr. Firouz Badrkhani Ajaei. His unwavering guidance and support at every stage of my thesis motivated me to make momentous progress on my research and generally in the field of electrical engineering.

I also want to thank the examining committee, Dr. Rajiv Varma, Dr. Jing Jiang, and Dr. Ayan Sadhu for their time and considerations. Finally, I want to thank my parents for their support of my higher education.

Table of Contents

Abstract.....	ii
Summary for Lay Audience.....	iii
Acknowledgments.....	v
Table of Contents.....	vi
List of Tables	viii
List of Figures.....	ix
List of Appendices	xii
List of Abbreviations	xiii
Nomenclature.....	xiv
Chapter 1	1
1 Introduction.....	1
1.1 Background.....	1
1.2 Statement of the Problem.....	3
1.3 Literature Review.....	4
1.4 Thesis Objectives	6
1.5 Methodology.....	6
1.6 Study System	8
1.7 Thesis Outline	9
Chapter 2	10
2 VSG Control and Current Limiting Strategies.....	10
2.1 Introduction.....	10
2.2 VSG Control	10
2.3 Small-Signal Stability Analysis	14
2.4 Current Limiting Strategies.....	19
2.4.1 Angle Priority.....	22

2.4.2	<i>d</i> -axis Priority.....	24
2.4.3	<i>q</i> -axis priority.....	26
2.5	Performance Evaluation.....	28
2.5.1	Validation of VSG Output Power in Saturation Mode.....	28
2.5.2	Comparison of Current Limiting Strategies.....	31
2.5.3	The Effect of Virtual Impedance on Transient stability.....	38
2.6	Conclusion.....	38
Chapter 3	39
3	Impacts of Damping on the VSG Transient Stability.....	39
3.1	Introduction.....	39
3.2	Theoretical Analysis.....	39
3.3	Performance Evaluation.....	41
3.4	Proposed Adaptive Damping Strategy.....	50
3.5	Conclusion.....	54
Chapter 4	55
4	Summary and Conclusions.....	55
4.1	Summary.....	55
4.2	Conclusion.....	55
4.3	Future Work.....	56
References	57
Appendices A: Study System Parameters	64
Appendices B: VSG Output Power Characteristics	66
Curriculum Vitae	69

List of Tables

Table 2. 1: VSG Parameters.....	16
Table 2. 2 Comparison of the different current limiting strategies.....	36
Table A. 1: Study system parameters	64
Table A. 2: Overhead line length.....	64
Table A. 3: Load specification.....	65

List of Figures

Figure 1. 1: Single-line diagram of the study system	8
Figure 2. 1: VSG model (a) VSG circuit and the voltage and current control loops (b) Governor model (c)AVR model	11
Figure 2. 2: Details of the VSG multiloop control system (a) abc to dq transformation (b) voltage control (c) current control	13
Figure 2. 3: Equivalent model of a grid-connected VSG.....	14
Figure 2. 4: Active power loop of the VSG	14
Figure 2. 5: Small-signal model of the active power loop.....	14
Figure 2. 6: Eigenvalues of the VSG for different values of D_p	18
Figure 2. 7: Step response of the VSG output power P_e for different values of D_p	18
Figure 2. 8: Eigenvalues of the VSG for different values of H	17
Figure 2. 9: Step response of the VSG output power P_e for different values of H	17
Figure 2. 10: Phasor diagram of dq reference frame	20
Figure 2. 11: Current limiting strategies (a) Angle priority (b) d -axis priority (c) q -axis priority.....	21
Figure 2. 12: Performance of the VSG utilizing the angle priority current limiting strategy (a) VSG power (b) VSG current (c) d -axis reference current (d) q -axis reference current (e) dq components of the grid voltages	23
Figure 2. 13: Performance of the VSG utilizing the d -axis priority current limiting strategy (a) VSG power (b) VSG current (c) d -axis reference current (d) q -axis reference current (e) dq components of the grid voltages	25

Figure 2. 14: Performance of the VSG utilizing the q -axis priority current limiting strategy (a) VSG power (b) VSG current (c) d -axis reference current (d) q -axis reference current (e) dq components of the grid voltages	27
Figure 2. 15: Single-line diagram of the study system illustrating the fault locations.	29
Figure 2. 16: Comparison of the VSG P - δ characteristics obtained based on theoretical analysis and time-domain simulation (a) angle priority (b) d -axis priority (c) q -axis priority	30
Figure 2. 17: Performance of the VSG based on the angle priority (a) VSG terminal voltages (at 27.6kV-side of transformer) (b) VSG terminal currents (at 27.6kV-side of transformer) (c) d -axis reference currents (d) q -axis reference currents (e) VSG angular speed (f) power angle	32
Figure 2. 18: Performance of the VSG based on the d -axis priority (a) VSG terminal voltages (at 27.6kV-side of transformer) (b) VSG terminal currents (at 27.6kV-side of transformer) (c) d -axis reference currents (d) q -axis reference currents (e) VSG angular speed (f) power angle.....	33
Figure 2. 19: Performance of the q -axis priority (a) VSG terminal voltages (at 27.6kV-side of transformer) (b) VSG terminal currents (at 27.6kV-side of transformer) (c) d -axis reference currents (d) q -axis reference currents (e) VSG angular speed (f) power angle	34
Figure 2. 20: The operating point trajectory of VSG subjected to a three-phase fault at F1 under different current limiting strategies.....	35
Figure 2. 21: Impacts of X_v on transient stability (a) angle priority (b) d -axis priority (c) q -axis priority	37
Figure 3. 1: Acceleration behavior of the VSG under a solid fault (a) VSG with negligible damping (b) VSG with small damping factor (c) VSG with large damping factor	40
Figure 3. 2: Single-line diagram of the study system with the location of fault.....	42
Figure 3. 3: Performance of the VSG with negligible damping under a three-phase fault at node N1 (a) VSG terminal voltages at 27.6kV-side of transformer (b) VSG terminal currents	

at 27.6kV-side of transformer (c) mechanical and electrical powers (d) acceleration and damping powers (e) VSG angular speed (f) power angle.....	43
Figure 3. 4: Operating point (state transition) trajectory of the VSG with negligible damping, subjected to a three-phase fault.....	44
Figure 3. 5: Performance of the VSG with small damping under a three-phase fault at node N1 (a) VSG terminal voltages at 27.6kV-side of transformer (b) VSG terminal currents at 27.6kV-side of transformer (c) mechanical and electrical powers (d) acceleration and damping powers (e) VSG angular speed (f) power angle.....	45
Figure 3. 6: Operating point (state transition) trajectory of the VSG with small damping, subjected to a three-phase fault.....	46
Figure 3. 7: Performance of the VSG with large damping under a three-phase fault at node N1 (a) VSG terminal voltages at 27.6 kV-side of transformer (b) VSG terminal currents at 27.6 kV-side of transformer (c) mechanical and electrical powers (d) acceleration and damping powers (e) VSG angular speed (f) power angle.....	48
Figure 3. 8: Operating point (state transition) trajectory of the VSG with large damping, subjected to a three-phase fault.....	49
Figure 3. 9: adaptive damping characteristics.....	50
Figure 3. 10: Performance of the VSG with adaptive damping factor under a three-phase fault (a) VSG terminal voltages (at 27.6kV-side of transformer) (b) VSG terminal currents (at 27.6kV-side of transformer) (c) mechanical and electrical powers (d) acceleration and damping powers (e) VSG angular speed (f) power angle.....	52
Figure 3. 11: The operating point trajectory of VSG with adaptive damping subjected to a three-phase fault.....	53
Figure 3. 12: Operating point trajectory of the VSG with different damping values	54

List of Appendices

Appendices A: Study System Parameters.....	64
Appendices B: VSG Output Power Characteristics.....	66

List of Abbreviations

AC	Alternating Current
BESS	Battery Energy Storage System
CCT	Critical Clearing Time
DC	Direct Current
DER	Distributed Energy Resource
ESS	Energy Storage System
HVDC	High-Voltage Direct Current
GCC	Grid-Connected Converter
LV	Low Voltage
MPPT	Maximum power point tracking
OS	Overshoot
PCC	Point of Common Coupling
PI	Proportional-Integral
PLL	Phase-Locked Loop
PV	Photovoltaic
SPWM	Sine Pulse Width Modulation
RES	Renewable Energy System
SG	Synchronous Generator
SM	Synchronous Machine
VI	Virtual Impedance
VSC	Voltage-Sourced Converter
VSG	Virtual Synchronous Generator
VSM	Virtual Synchronous Machine

Nomenclature

P_0	Active power reference
Q_0	Reactive power reference
P_e	Measured output active power
Q_e	Measured output reactive power
P_m	Mechanical input power reference
P_{um}	Active power in unsaturated mode
P_{sm}	Active power in saturated mode
E_0	Nominal voltage
ω_0	Nominal angular frequency
ω_m	Virtual rotor angular frequency
ω_g	Grid angular frequency
θ_m	Virtual rotor phase angle
δ	Power angle
V	Voltage at PCC
E_{ref}	Virtual internal electromotive force
L_f	Inductance of the LC filter
C_f	Capacitance of the LC filter
H	Inertia constant
J	Moment of inertia
D_p	Damping factor
R_v	Virtual resistance and reactance
X_v	Virtual reactance
Z_g	<i>Grid impedance</i>
v_{grid}	Grid voltages and currents
i_{grid}	Grid voltages and currents

I_{max}	Maximum allowable current magnitude
I_{mag}	Current magnitude
k_p	ω - P droop coefficient
k_q	Q - V droop coefficient
d	d -axis components
q	q -axis components
e_d	d -axis VSG voltage
e_q	q -axis VSG voltage
v_d	d -axis grid voltage
v_q	q -axis grid voltage
i_d^{ref*}	d -axis current reference before current limiting
i_d^{ref}	d -axis current reference after current limiting
i_q^{ref*}	q -axis current reference before current limiting
i_q^{ref}	q -axis current reference after current limiting
ξ	damping ratio
t_c	clearing time
δ_{cr}	critical clearing angle

Chapter 1

1 Introduction

1.1 Background

Distributed Energy Resources (DERs) have been increasingly integrated in power systems [1]. The majority of these DERs are interfaced to the grid using Voltage Sourced Converters (VSCs) [2]. The large-scale utilization of the inverter-interfaced DERs leads to lack of inertia which brings considerable concerns about grid stability [1], [3].

The large inertia of the Synchronous Machine (SM) -based traditional power generation systems [4] is usually desired as it can slow down the dynamics and reduce the frequency deviations [2]. For the SGs, as there is mechanical-rotating mass, large physical inertia may be readily available to buffer the system dynamic responses. In contrast, for the grid-connected converters without mechanical rotors, either additional devices should be adopted or the control should be retrofitted to provide (virtual) inertia, i.e., absorb, or compensate for the transient energy; otherwise, the system may collapse under severe disturbances [3]. To emulate inertia, energy storage units should be employed and properly regulated to release or absorb energy in the same way as the rotors of SGs do. To achieve so, several virtual inertia solutions have been introduced in the literature, which will be reviewed in the following.

- 1) Virtual Synchronous Generator With ESS: An effective way of providing inertia support to the grid is to control the power electronic converters to mimic the behavior of SGs, i.e., release the stored energy to damp the disturbances when needed. The grid-connected power converters operating in this way are referred to as virtual synchronous machines (VSMs) or virtual synchronous generators (VSGs) [5]-[15]. In this case, the inertia can be emulated and also directly adjusted, which makes it possible and flexible to use the emulated (virtual) inertia to stabilize the entire system [16]-[20]. It should be noted that the virtual inertia of a VSG is limited by the ESS performance, e.g., batteries or supercapacitors [3], [21]. The drastic

development of ESS technologies is promoting the ESS as more viable and popular solutions for inertia support and primary frequency regulation in the future [3], [22].

- 2) **Virtual Inertia From the DC-Link Capacitor:** The lack of inertia can partially be compensated through proper control of the DERs [1]. Some attempts have been made to seek the balance between inertia emulation and control flexibility. Instead of completely modifying the control of grid-connected converters [3], the dc-link capacitor, as an energy storage device, can be utilized to provide virtual inertia [23], [24]. This method can easily be implemented without increasing the system cost and complexity. Without additional ESS units, the virtual inertia can be emulated by charging and discharging the dc-link capacitor [23], [25]. Although the dc-link capacitor is generally unable to deal with large energy storage, it enables flexible frequency support from all power converters, especially in small-scale and relatively weak grids. To achieve the inertia emulation by the dc-link capacitor, the dc-link voltage control should be modified. When there is energy unbalance in the grid, the dc-link voltage will be regulated in a way to process the energy flow (i.e., emulating the inertia to stabilize the system). During this process, the energy unbalance is compensated, and the virtual inertia is generated by the dc-link capacitor. Clearly, the dc-link voltage control used to simulate the virtual inertia can be the conventional multiloop control with minor modifications [26], the dc-link voltage-frequency droop control [2], or the self-synchronized dc-link voltage control [27].
- 3) **Inertia Emulating Control of Renewable Energies:** In addition to the virtual inertia from ESSs or dc-link capacitors, inertia can be provided from renewable energy sources. For wind turbine systems, especially the DFIG systems, the virtual inertia can be provided by recoupling the rotor mass to the grid frequency [28]-[32]. More specifically, for the latter solution, the inertia can be generated by the rotating mass of the DFIG (i.e., control the rotor motion). In this case, a frequency response loop in the MPPT loop of the rotor-side converter should be introduced, and the active power reference can be adjusted following the grid frequency deviation [3], [28], [33]. As the DFIG is operating in the MPPT mode in steady state, the inertia from

the rotor motion can only deal with under-frequency conditions [34]. The inertia emulating is also applicable to PV systems, where the ESS or dc-link capacitor-based inertia provision is also feasible [35]-[37]. In this case, the PV system keeps running in the MPPT mode and is barely affected by the frequency deviation, i.e., the PV system is operating as a constant current source without any grid support function. However, the output power of PV systems is fluctuating, and the frequent charging and discharging of energy storage devices (e.g., batteries and dc-link capacitors) are impractical and not economic-friendly. Thus, how to afford the virtual inertia by flexible PV output power control is of interest.

VSGs suffer from some of the issues that affect the operation of the SG [13], [38], [39]. One of the most challenging issues is the transient stability of the VSG. In traditional power systems, the transient stability is the ability of the SGs to maintain their synchronism when subjected to faults [4]. Likewise, prolonged exposure to faults may cause instability and disconnection of VSGs [40], [41]. To maintain transient stability, a fault must be cleared before the SG power angle (VSG virtual power angle) exceed a specific limit. However, according to the fault ride through (FRT) requirements set by different grid codes [40], [42], the DERs, including those that are controlled as VSGs, may be required to remain connected to the grid for a time period after faults take place [38], [43], [44]. In specific applications such as microgrids, such DERs may be required (or at least are preferred) to continue to operate even beyond the FRT requirements [43]-[45]. Many attempts have been made to advance the VSG technology, typically considering the inertia and damping characteristics [12], [46], stability issues [47], [48], operational modes (islanded and grid-connected) [49] and general control strategies [50]. However, the transient stability of the VSG has not been comprehensively investigated.

1.2 Statement of the Problem

As compared to the SGs that can supply large fault currents, inverters have significantly smaller current limits [44]. Therefore, the control system of the VSG should effectively limit the associated inverter current, which can be achieved using different strategies. Although the inverter current limit has been reported to impact the VSG transient stability

[27], [51]-[53], the existing literature has not investigated the effects of different current limiting strategies on the transient stability of the VSG.

Another important parameter that affects the transient stability of the VSG is its damping factor [54]. For a physical SM, a small damping is often provided by the damper windings and also caused by friction [1], [4]. The versatile control system of the state-of-the-art VSG technology enables implementing arbitrary amounts of virtual damping and inertia, as long as the DC-link has the capacity to provide or absorb the associated virtual kinetic energy. The effects of virtual damping on the transient stability of the VSG have not been investigated in detail. There is a need for clear and comprehensive guidelines regarding the choice of the VSG virtual damping factor that would ensure transient stability under the expected fault conditions.

1.3 Literature Review

If a converter becomes unstable after a large disturbance, it has to be disconnected from the grid [55]. With the increased penetration of DERs in power systems, it is becoming more and more crucial for the grid-forming converters to remain connected to and support the grid during and after faults [44]. Since the VSG does not utilize a PLL for grid synchronization, it suffers from transient stability issues, i.e., can become unstable after prolonged faults [40], [41]. Different aspects of the VSG transient stability have been investigated in [13], [27], [38], [39], [41], [44], [51]-[53], [56]-[62]. It has been reported that the transient stability of the VSG is affected by its current limit [27], [38], [41], [44], [51]-[53], [58]-[60]. Power electronic converters can only handle 20%–40% overcurrent stress and thus have to be protected against extreme events such as short circuits [44], [63]. However, the impacts of different inverter current limiting strategies on the VSG transient stability has not been comprehensively investigated in the existing technical literature.

The impact of inverter current limiting is neglected in the VSG transient stability studies reported in [13], [39], [56], [57], [61], [64], [62]. The inverter current limiting can be achieved using virtual impedance (VI) [38], [41], [44], [58]-[60], [65], [66]. A large virtual impedance enables limiting the current transients, while maintaining the voltage

source nature of the inverter. However, a large virtual impedance may cause poor dynamic response to disturbances.

A more versatile option is the dq reference frame-based multiloop control structure [27], [51]-[53] which uses an outer voltage control loop that provides the limited current references to an inner current control loop. In a VSG utilizing a multiloop control structure, the references of the outer voltage control loop, i.e., the voltage magnitude and angle references, are determined based on the virtual electromechanical model of the VSG [38]. This control structure enables effectively limiting the inverter currents while prioritizing the d-axis current, q-axis current, or the virtual power angle of the VSG [67]. Unlike the virtual impedance-based current limiting strategy, the multiloop control system effectively limits the VSG current independent of the virtual impedance value and also enables prioritizing the d-axis current, q -axis current, or the virtual power angle of the VSG in the current limiting state. Hence, the studies of this thesis are focused on the VSG utilizing a dq -framed based multiloop control which is also able to implement the virtual impedance [68]-[70].

In addition to the current limiting characteristic, which is discussed in Chapter 2, parameters such as the inertia, damping, and virtual reactance affect the VSG transient stability. Since the main goal of operating an inverter as a VSG is inertia emulation, the inertia is not a parameter that can be significantly changed. However, the other two parameters could be determined so as to enhance the VSG transient stability. The damping factor considerably affects the transient stability of the VSG [27], [39], [44], [51], [56], [59], [62]. The impacts of different damping values on the VSG transient stability has not been comprehensively investigated in the existing technical literature. Switching between low and high damping values using an adaptive algorithm has been proposed in [27]. This strategy requires a triggering algorithm that decides when the switching is needed and also does not provide desirable dynamic response (due to sudden variations of the Damping factor).

1.4 Thesis Objectives

The main objectives of this research are (i) investigating the impacts of current limiting strategies on the VSG power output ($P - \delta$) characteristics, (ii) identifying the most suitable current limiting strategy for improved transient stability, (iii) investigating the impacts of the VSG parameters, i.e., virtual inertia, virtual damping, and virtual reactance, on its the transient stability, and (iv) developing an adaptive control strategy that improves the VSG transient stability through continuous adjustment of those parameters.

1.5 Methodology

In order to achieve the thesis objectives:

- The studies are conducted using a realistic study system which is the benchmark Canadian rural distribution network [71]. The study system is developed using detailed models of its components. The VSG is represented by a switching-type inverter and the associated multiloop control systems.
- To verify small signal stability and ensure desirable dynamic response of the VSG to disturbances, the appropriate values of the VSG parameters are determined based on eigenvalue analysis.
- Off-line time-domain simulation studies are performed in the PSCAD-EMTDC software environment to investigate the transient response of the VSG to faults and disturbances.
- Comprehensive theoretical and simulation studies are conducted to investigate the impacts of the inverter current limiting strategies as well as the virtual damping factor and the virtual reactance on the transient stability of the VSG. Numerous fault studies are conducted to evaluate the effects of different damping values on the critical clearing time of faults.
- The results of these studies are used to identify the best current limiting strategy and also to develop and validate an advanced damping control strategy that improves the transient

stability of the VSG and increases the critical clearing time of faults in a system containing VSGs.

- An adaptive damping control system for enhanced transient stability of the VSG is proposed and verified.

1.6 Study System

The simulation studies in this research are conducted using a realistic study system that represents the 27.6 kV Canadian rural distribution network described in [71]. Figure 1.1 shows the single-line diagram of the study system. The study system parameters are provided in Appendix A.

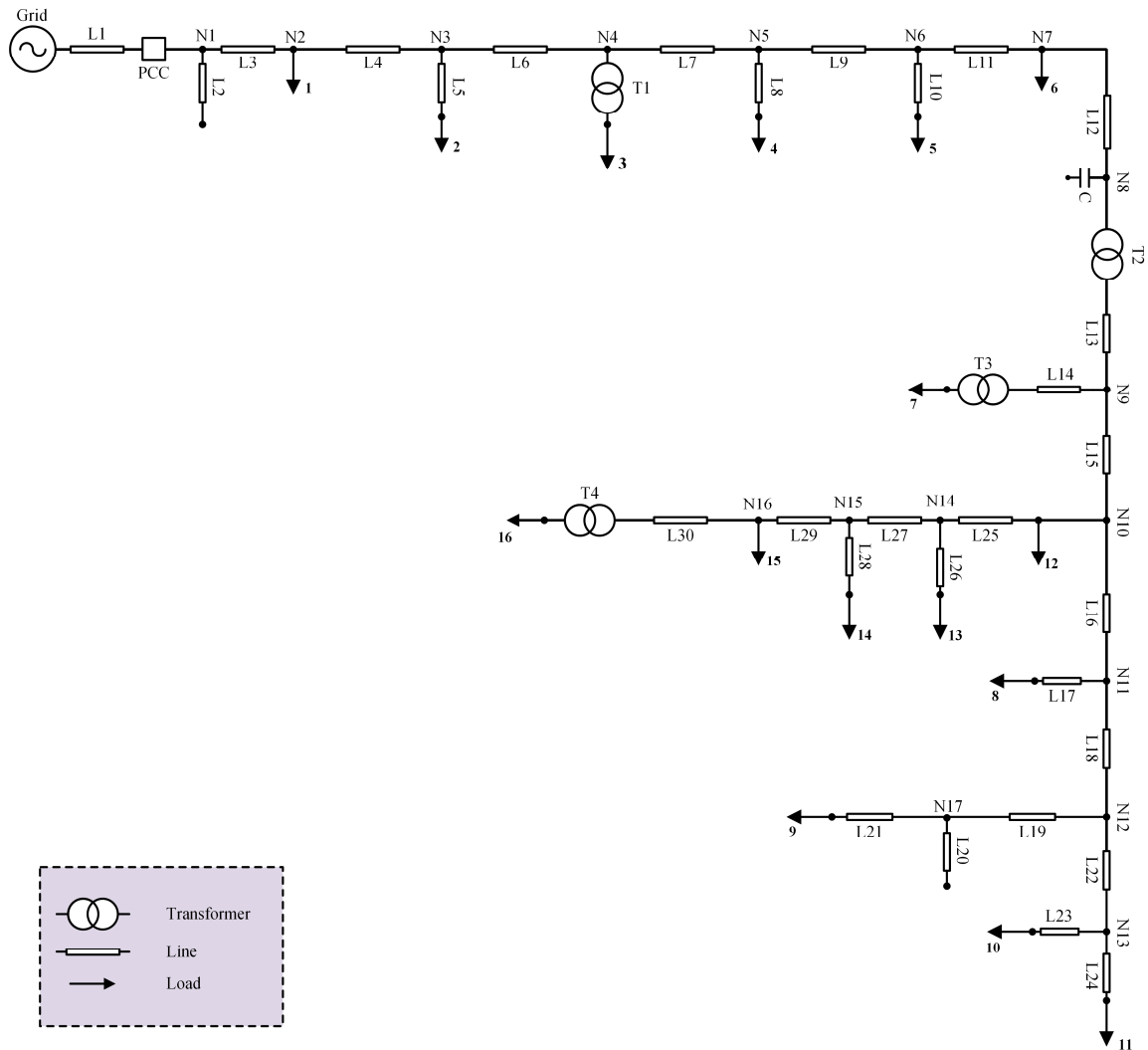


Figure 1. 1: Single-line diagram of the study system

1.7 Thesis Outline

The next chapters of this thesis are organized as follows:

- Chapter 2 gives an overview of the VSG control systems and investigates and compares the impacts of different current limiting strategies on the transient stability of the VSG. The most suitable current limiting strategy for improving transient stability is identified and, the impacts of the VSG parameters on its the transient stability will be investigated.
- Chapter 3 presents the acceleration behavior of the VSG with different damping value, under fault disturbances, to evaluate the effects of different damping values on the critical clearing time of faults. In addition, an adaptive damping control system for enhanced transient stability of the VSG is proposed.
- Chapter 4 summarizes the thesis contributions and provides concluding remarks.

Chapter 2

2 VSG Control and Current Limiting Strategies

2.1 Introduction

This chapter provides a brief overview of the VSG control systems. To verify small signal stability and ensure desirable dynamic response of the VSG to disturbances, the appropriate values of the VSG parameters are determined based on eigenvalue analysis. Subsequently, different current limiting strategies are theoretically and numerically investigated in terms of their impacts on the transient stability of the VSG by calculating the critical clearing times of faults. Extensive simulation studies are carried out to verify the validity of the theoretical analysis and the effects of the current limiting strategies on transient stability of the VSG under various disturbances.

2.2 VSG Control

Figure 2.1 illustrates a typical three-phase VSG and a high-level view of the corresponding multiloop control structure. The VSG circuit typically consists of a DER, a voltage-sourced converter (VSC), a harmonic filter and an interface transformer. The VSG control system includes the voltage and current control loops, the electromechanical model of a SG, i.e., the swing equation of (2.1), and the governor and AVR models, as shown in Figure 2.1(b) [14], [38], [51], [56], [59], [68], [72]-[74] and Figure 2.1(c) [41], [27], [51], [52], [75]-[77], respectively. The reference phase angle and magnitude of the VSG internal voltage phasor, i.e., θ_m and E_{ref} , are determined by the electromechanical model of Figure 2.1 (b) and the AVR of Figure 2.1 (c).

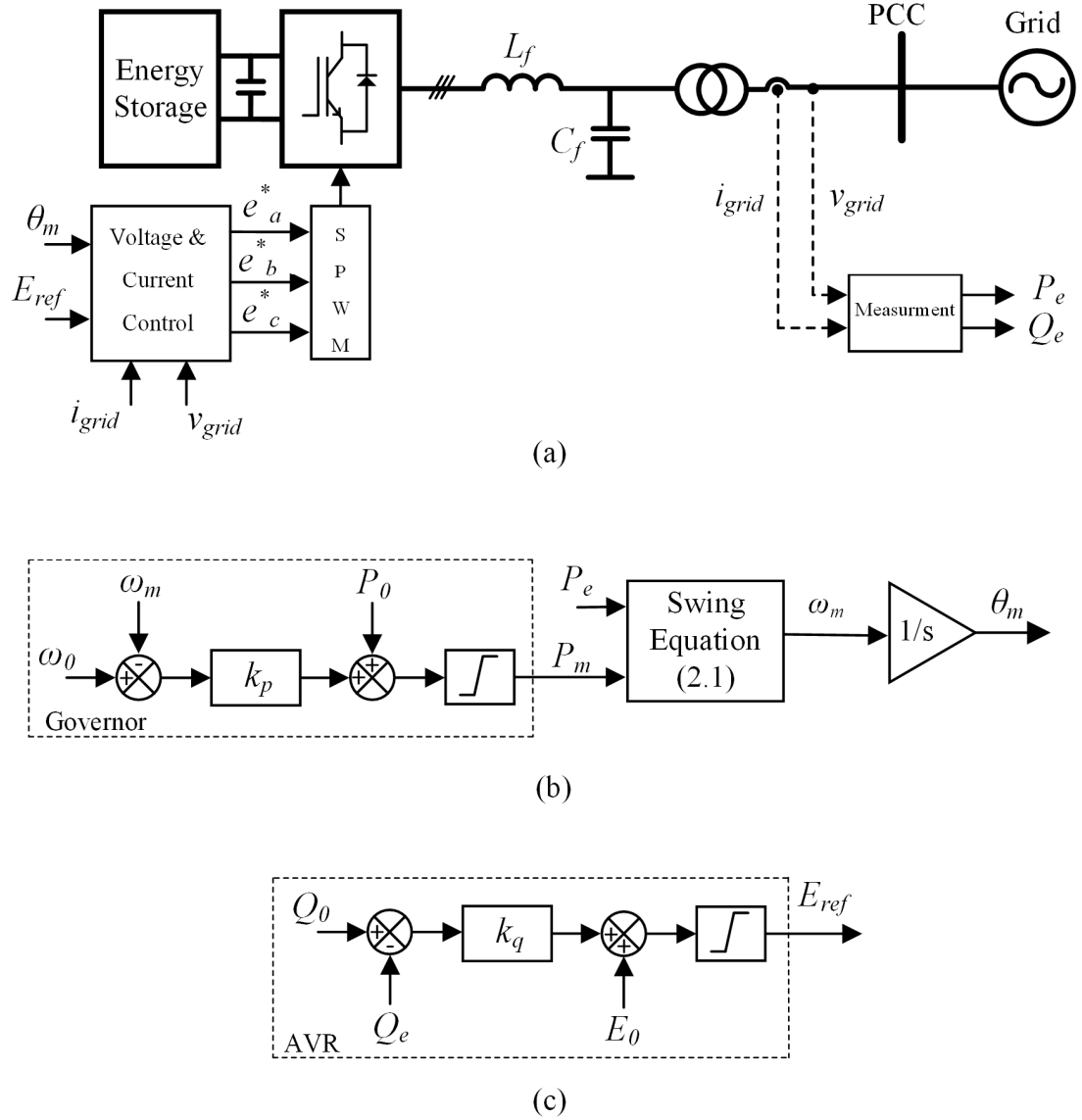


Figure 2. 1: VSG model (a) VSG circuit and the voltage and current control loops (b) Governor model (c)AVR model

The virtual electromechanical model is represented by the following equations [68], [59]:

$$P_m - P_e = J\omega_m \frac{d\omega}{dt} + D_p(\omega_m - \omega_0) \quad (2.1)$$

$$\theta_m = \int \omega_m dt \quad (2.2)$$

$$k_q(Q_0 - Q_e) + E_0 = E_{ref} \quad (2.3)$$

The mechanical part of the machine is governed by (2.1) where J is the moment of inertia of all parts rotating with the rotor, P_m is the mechanical input power, P_e is the electromagnetic output power and D_p is the virtual damping factor. The damping factor D_p in the swing equation actually plays the role of the frequency droop control and hence it is called the frequency droop coefficient as well. The term k_q serves the purpose of voltage droop control.

As a result, a synchronverter is able to take part in the regulation of system frequency and voltage. It was shown in [78] that the commonly needed phase-locked loop can be removed so it is not shown in the controller.

Mimicking a SG, the virtual moment of inertia J is:

$$J = \frac{2HS_{base}}{\omega_0^2} \quad (2.4)$$

where H is the machine inertia constant and S_{base} is the base power of the machine.

The VSG multiloop control system consists of a current limiter, as well as voltage and current control loops represented in the rotating reference frame that is locked on the VSG virtual rotor angle [68], [79]. The voltage and current control loops utilize proportional-integral (PI) controllers and feedforward decoupling terms. The virtual impedance is implemented in the outer voltage control loop which determines the current reference as follows [68]. The current reference can be calculated as (2.5).

$$\begin{bmatrix} e_d \\ e_q \end{bmatrix} = \begin{bmatrix} v_d \\ v_q \end{bmatrix} + \begin{bmatrix} L_v p + R_v & -\omega L_v \\ \omega L_v & L_v p + R_v \end{bmatrix} \begin{bmatrix} i_d^{ref*} \\ i_q^{ref*} \end{bmatrix} \quad (2.5)$$

where $p = d/dt$, which is the differential operator; L_v and R_v represent the virtual inductance and resistance, respectively which includes the total impedance from the VSG to the grid. The simplified representation of a grid-connected VSG is shown in Figure 2.3. In the frequency domain, (2.5) is transformed to:

$$\begin{bmatrix} I_d^{ref*}(s) \\ I_q^{ref*}(s) \end{bmatrix} = \begin{bmatrix} L_v s + R_v & -\omega L_v \\ \omega L_v & L_v s + R_v \end{bmatrix}^{-1} \begin{bmatrix} E_d - V_d \\ E_q - V_q \end{bmatrix} \quad (2.6)$$

which can be simplified as (2.7).

$$\begin{bmatrix} I_d^{ref*}(s) \\ I_q^{ref*}(s) \end{bmatrix} = \frac{1}{(L_v s + R_v)^2 + (\omega L_v)^2} \begin{bmatrix} (L_v s + R_v)(E_d - V_d) + \omega L_v(E_q - V_q) \\ (L_v s + R_v)(E_q - V_q) - \omega L_v(E_d - V_d) \end{bmatrix} \quad (2.7)$$

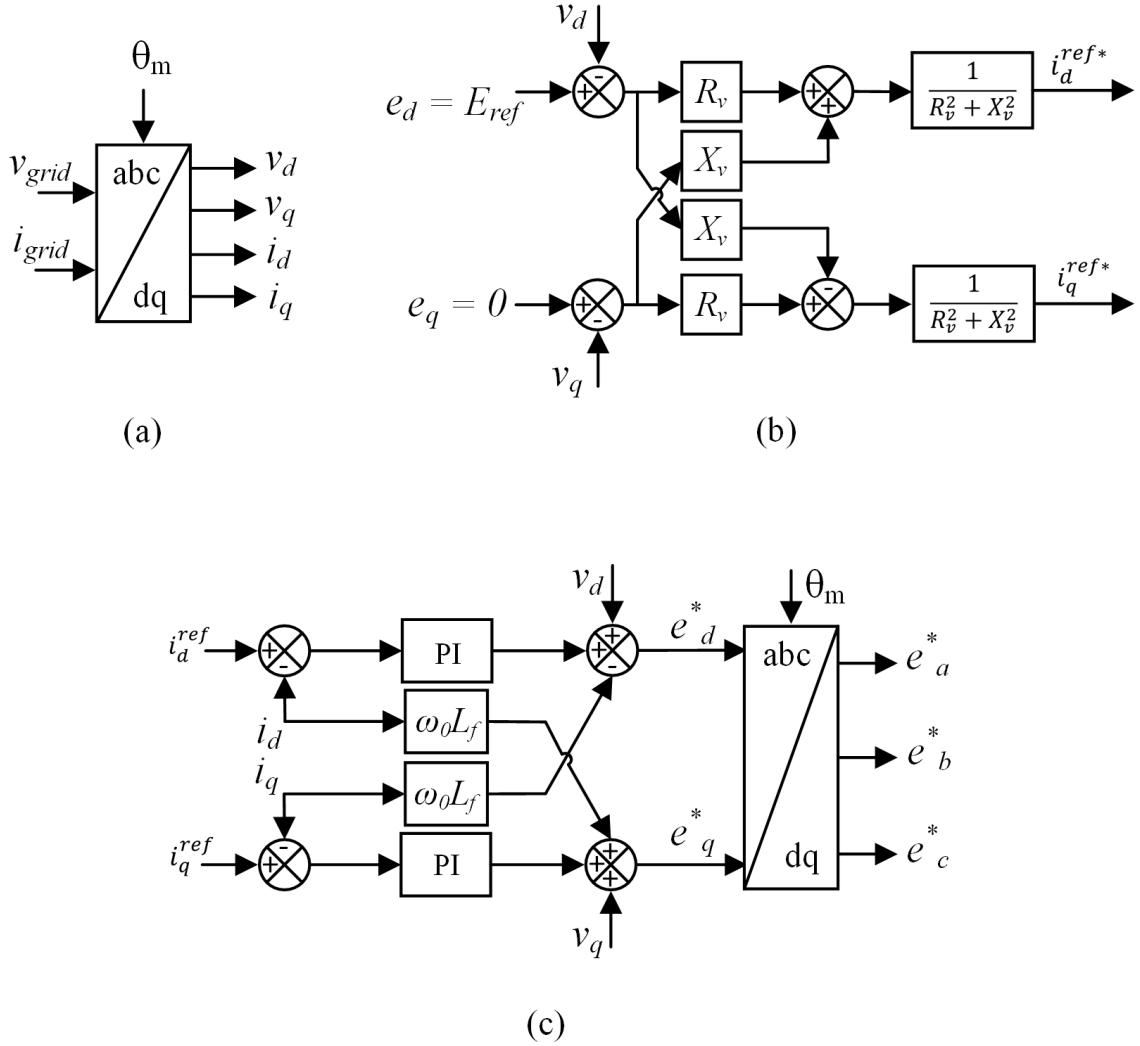


Figure 2. 2: Details of the VSG multiloop control system (a) abc to dq transformation (b) voltage control (c) current control

Based on the Laplace final-value theorem, the current reference can be deduced from (2.7) as follows.

$$\begin{bmatrix} i_d^{ref*} \\ i_q^{ref*} \end{bmatrix} = \frac{1}{R_v^2 + X_v^2} \begin{bmatrix} R_v(e_d - v_d) + X_v(e_q - v_q) \\ R_v(e_q - v_q) - X_v(e_d - v_d) \end{bmatrix} \quad (2.8)$$

Equation (2.8) represents the virtual impedance in the outer voltage control loop of Figure 2.3 (b).

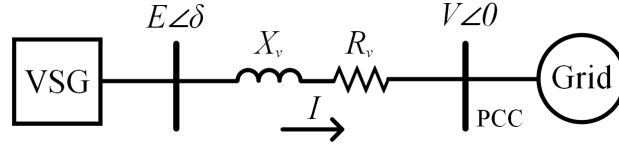


Figure 2.3: Equivalent model of a grid-connected VSG

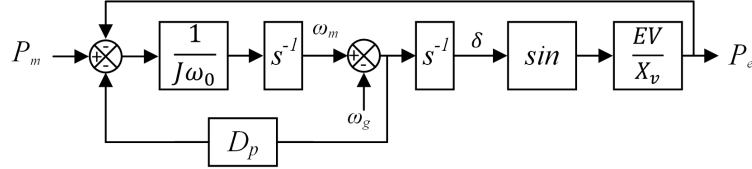


Figure 2.4: Active power loop of the VSG

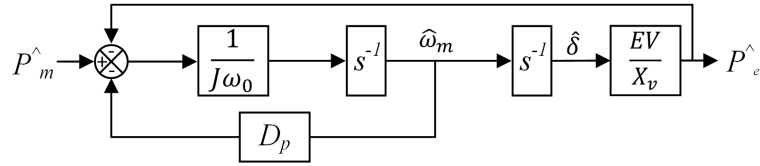


Figure 2.5: Small-signal model of the active power loop

Figure 2.3 shows a simplified representation of the VSG connected to the grid, where E represents the internal voltage of VSG that is connected to the grid at the point of common coupling through virtual resistance and reactance. According to Figure 2.3, the VSG output power is expressed by (2.9) [72], [76], [80].

$$P_e = \frac{E}{R_v^2 + X_v^2} (X_v V \sin \delta + R_v (E - V \cos \delta)) \quad (2.9)$$

Since the virtual impedance is mainly inductive ($X_v \gg R_v$), (2.9) can be written as (2.10).

$$P_e = \frac{EV}{X_v} \sin \delta \quad (2.10)$$

2.3 Small-Signal Stability Analysis

According to [6], [81], the coupling terms between the active power loop and the reactive power loop can be ignored. Therefore, the parameters of each loop can be designed independently, which greatly simplify the design procedure. The VSG active power loop

can be simply represented, as shown in Figure 2.4. Figure 2.5 shows the small-signal model of the active power loop [6], [77], [81]-[83]. Based on this model, the transfer function of the VSG is obtained as (2.11) and the poles can be calculated as (2.12).

$$\frac{P_e}{P_m} = \frac{EV}{JX_v\omega_0s^2 + X_vD_p s + EV} \quad (2.11)$$

$$s_{1,2} = \frac{-D_p \pm \sqrt{D_p^2 - \frac{4J\omega_0EV}{X_v}}}{2J\omega_0} \quad (2.12)$$

According to (2.11), the peak time t_p , settling time t_s , overshoot OS , and damping ratio ξ can be calculated as follows:

$$t_p = \frac{2\pi J\omega_0}{\sqrt{\frac{4J\omega_0EV}{X_v} - D_p^2}} \quad (2.13)$$

$$OS = 100 \times e^{-\frac{\pi D_p}{\sqrt{\frac{4J\omega_0EV}{X_v} - D_p^2}}} \% \quad (2.14)$$

$$t_s = \frac{8J\omega_0}{D_p} \quad (2.15)$$

$$\xi = \frac{D_p}{2} \sqrt{\frac{X_v}{J\omega_0EV}} \quad (2.16)$$

To investigate the impacts of damping, a derivative of t_p with respect to D_p is taken. According to (2.13), $\frac{dt_p}{dD_p} > 0$.

$$\frac{dt_p}{dD_p} = \frac{2\pi J\omega_0 D_p}{\sqrt{\left(\frac{4J\omega_0EV}{X_v} - D_p^2\right)^3}} > 0. \quad (2.17)$$

Similarly, $\frac{d(OS)}{dD_p} > 0$ and $\frac{dt_s}{dD_p} < 0$. Therefore, when the damping factor rises, the peak time increases, while the overshoot and settling time decrease.

The equation (2.12) indicates that the poles are affected by D_p , and J and X_v . If the parameters are chosen improperly, the poles will be too close to the imaginary axis which will cause poor dynamic response and stability issues. Therefore, in order to study the effects of the VSG damping on the dynamic response of the VSG, e.g., the response time, overshoot, and settling time, the appropriate values of the VSG parameters need to be

determined based on eigenvalue analysis.

The relationship between damping ratio ξ , and the *OS* is defined by (2.18) [4].

$$\xi = \frac{-\ln(OS)}{\sqrt{\pi^2 + \ln^2(OS)}} \quad (2.18)$$

By substituting (2.4) into (2.16), the damping factor can be determined in terms of the main parameters of the VSG as follows.

$$D_p = 2\xi \sqrt{\frac{2H\omega_0}{X_v}} \quad (2.19)$$

For the VSG, the value of the inertia constant H is typically chosen from 1.5 s to 6 s similar to that of a conventional SG [84]. The most commonly used value is 4 s [7], [17], [38], [56], [85]-[90]. According to (2.18), to limit the *OS* to less than 10%, the damping ratio ξ should be larger than 0.59. By substituting these values in (2.19), the desirable range for the damping factor is obtained to be $D_p > 92 \text{ p.u.}$.

A sensitivity analysis is conducted to investigate the effect of damping factor and inertia on the VSG dynamics and stability and to verify the above calculations. The VSG model parameters are given in Table 2.1. The eigenvalue analysis is conducted by fixing either H or D_p and changing the other parameter to investigate its effect on stability.

Figures 2.6 shows the results of the eigenvalue analysis a of the VSG output power, for different values of damping factor (D_p) while $H = 4 \text{ s}$. Figures 2.7 shows the results of the step response of the VSG output power with the same damping factors when the input mechanical power (P_m) increases from 0 to 1 p.u.

Table 2. 1: VSG Parameters

ω_0	$2\pi \times 60 \text{ rad/s}$
V	27.6 kV L-L
L_f	$6.4 \text{ }\mu\text{H}$
C_f	1.2 mF
X_v	0.5 p.u.
R_v	0.01 p.u.
S_{base}	2 MVA
P_m	2 MVA
H	4 s
I_{max}	1.5 p.u.
D_p	92 p.u.
k_p, k_q	$0, 0.05 \text{ p.u.}$

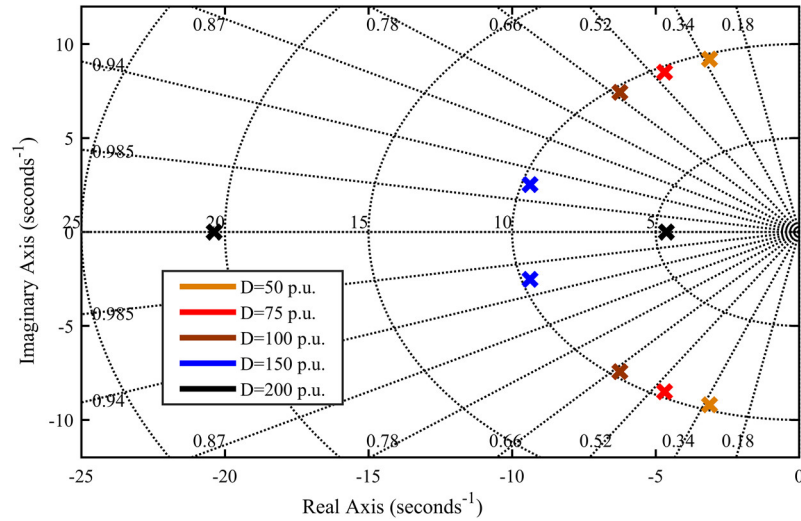


Figure 2. 6: Eigenvalues of the VSG for different values of D_p

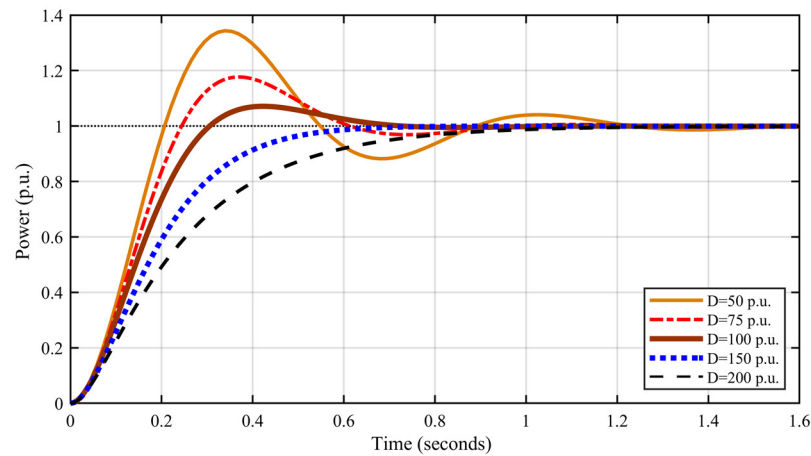


Figure 2. 7: Step response of the VSG output power P_e for different values of D_p

As shown in Figure 2.6, by decreasing the damping factor the poles will be too close to the imaginary that is not desirable. As shown in Figure 2.7, by increasing the damping value, the overshoot and settling time will be decreased. Therefore, a larger damping factor (D_p) result in a better output active power dynamic performance with lower oscillations but slower response. For extremely large damping value (black curve), the system is overdamped, and the dynamics of the system are too slow. Therefore, a damping factor around 100 is desirable (the brown curve). To be exact, a damping factor of 92 p.u. results in 10% overshoot. Therefore, this value chosen as the damping factor.

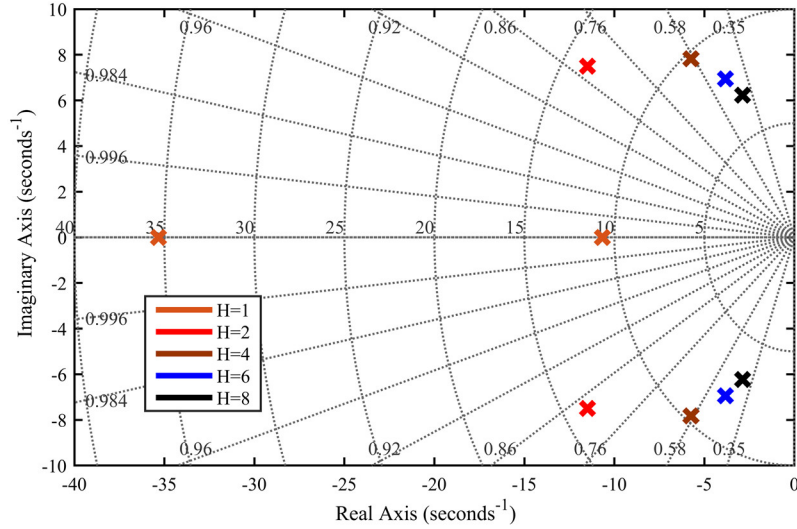


Figure 2. 8: Eigenvalues of the VSG for different values of H .

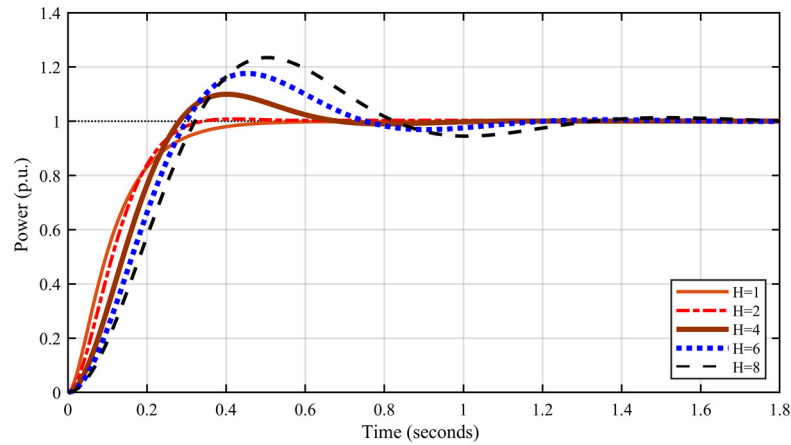


Figure 2. 9: Step response of the VSG output power P_e for different values of H

To study the impacts of the inertia constant, the damping factor is assumed to be fixed at 92 p.u. Figures 2.8 shows the results of the eigenvalue analysis a of the VSG output power, for different values of inertia constant (H) and Figures 2.9 shows the results of the step response of the VSG output power with the same inertia constants when the input mechanical power (P_m) increases from 0 to 1 p.u.

As shown in Figure 2.8, by increasing the inertia constant the poles will be too close to the imaginary axis which will cause poor dynamic response and stability issues. In addition, as shown in Figure 2.9, the overshoot and settling time will be increased by increasing the

inertia constant. An H value below 4 s leads to a more desirable dynamic response, that is, smaller overshoot and settling time. However, further reducing the inertia is counterproductive since the main goal of using a VSG is to emulate inertia. Therefore, these analysis shows that the inertia constant of 4s and damping factor of 92 p.u. (brown curve) provides desirable step response.

The eigenvalue studies are used to design the VSG by choosing the appropriate values for its parameters from small-signal stability perspective. The eigenvalue analysis is not used to investigate the transient stability. The transient stability of the VSG will be investigated based on the numerical analysis in the next part.

2.4 Current Limiting Strategies

To avoid excessive current flowing through the converter, the magnitude of the current reference signals are limited by the current limiter [51], [27] [52][53]. The multiloop control strategy of Figure 2.2 aligns the d -axis of the dq reference frame with the virtual rotor angle δ by setting the q -axis voltage reference e_q at zero and the d -axis voltage reference e_d equal to the VSG internal voltage magnitude E_{ref} (as shown in Figure 2.10).

As you can see in the Figure 2.10, the VSG current (I) is a vector on the Real-Imaginary plane. The components of this vector on the dq axis are called i_d and i_q . The magnitude of (I) should be limited by limiting i_d and i_q .

When the inverter current is saturated ($I_{mag} > I_{max}$), the VSG operates as a current source with $|i_{dq}^{ref}| = I_{max}$. Limiting the magnitude of the current reference vector $|i_{dq}^{ref}|$ can be achieved based on different strategies, namely the angle priority, d -axis priority and q -axis priority, as graphically illustrated in Figure 2.11. All three strategies ensure that the magnitude of the total current reference vector does not exceed the limit I_{max} . Thus, when the inverter current hits the limit, the following relationship applies to the dq current components obtained based on each of the three priorities.

$$|i_{dq}^{ref}| = \sqrt{(i_d^{ref})^2 + (i_q^{ref})^2} = I_{max} \quad (2.20)$$

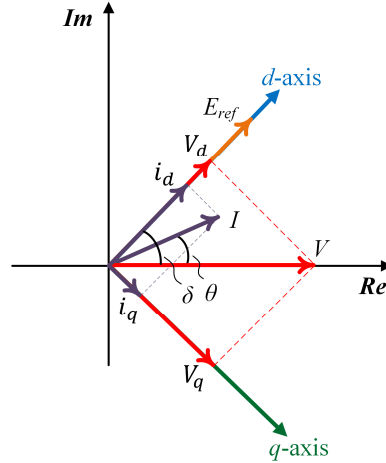


Figure 2. 6: Phasor diagram of dq reference frame

Regardless of the current limiting strategy, the VSG active power is calculated by

$$P_e = v_d i_d + v_q i_q \quad (2.21)$$

where the components of the grid voltage space vector in the dq reference frame are as follows.

$$v_d = V \cos \delta, \quad v_q = V \sin \delta \quad (2.22)$$

The current limiting strategies of Figure 2.11 have different impacts on the VSG output power determined by (2.21), because they lead to different values of i_d and i_q in the saturated mode. As a result, the VSG transient stability is affected by its current limiting strategy, as demonstrated in the following parts.

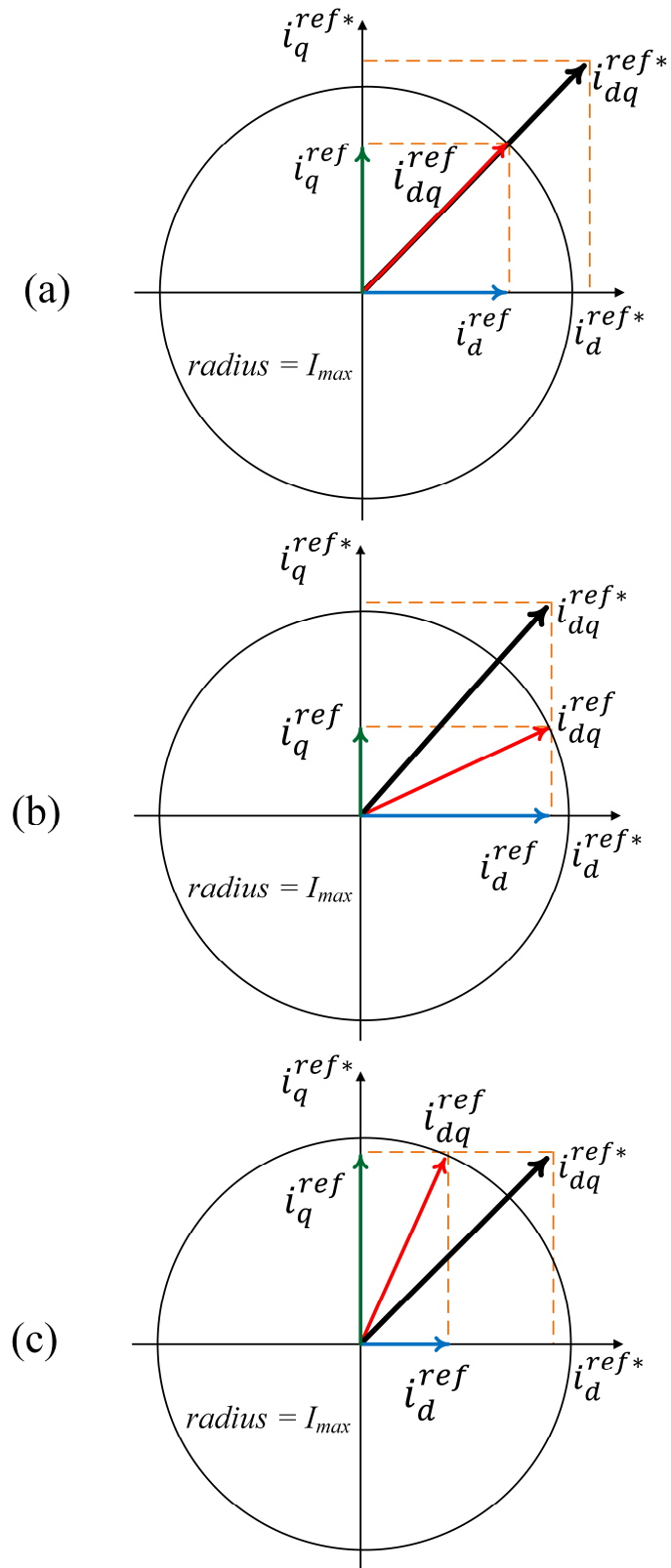


Figure 2. 7: Current limiting strategies (a) Angle priority (b) d -axis priority (c) q -axis priority

2.4.1 Angle Priority

Figure 2.11(a) shows the current limiting strategy that prioritizes the VSG current angle, which is shortly referred to as the angle priority. In this strategy, the dq components of the current reference vector $|i_{dq}^{ref}|$ are determined by (2.23) such that the inverter current magnitude does not exceed the maximum allowable level I_{max} and the current angle remains unchanged [44], [91]-[97]. The VSG output power when the angle priority is adopted can be calculated by (2.24). The Appendix B provides a detailed proof of this formula. Figure 2.12 shows how the angle priority current limiting strategy affects the $P - \delta$ characteristic of the VSG and its transient stability margins. Assuming that the VSG input power (virtual mechanical power P_m) is constant and equal to 1 p.u., which represents the worst case scenario, the VSG has two equilibrium points A and B. Small perturbation analysis shows that A is a stable equilibrium while B is an unstable one.

The difference between point A and B is the stability margin of the VSG. If a fault happens, the VSG starts to accelerate, and the operating point starts to move from point A towards B. If the fault has not been cleared fast enough and the angle reaches to point B, the systems became unstable. Thus, the point B is my critical clearing angle (δ_{cr}). The time that the VSG takes to go from point A to point B is the critical clearing time (CCT).

$$|i_d^{ref}| = \min \left(|i_d^{ref*}|, |i_d^{ref*}| \times \frac{I_{max}}{\sqrt{(i_d^{ref*})^2 + (i_q^{ref*})^2}} \right) \quad (2.23)$$

$$P_e = \begin{cases} \frac{EV}{x_v} \sin \delta & , |i_{dq}^{ref*}| < I_{max} \\ I_{max} \cos \frac{\delta}{2} & , O.W \end{cases} \quad (2.24)$$

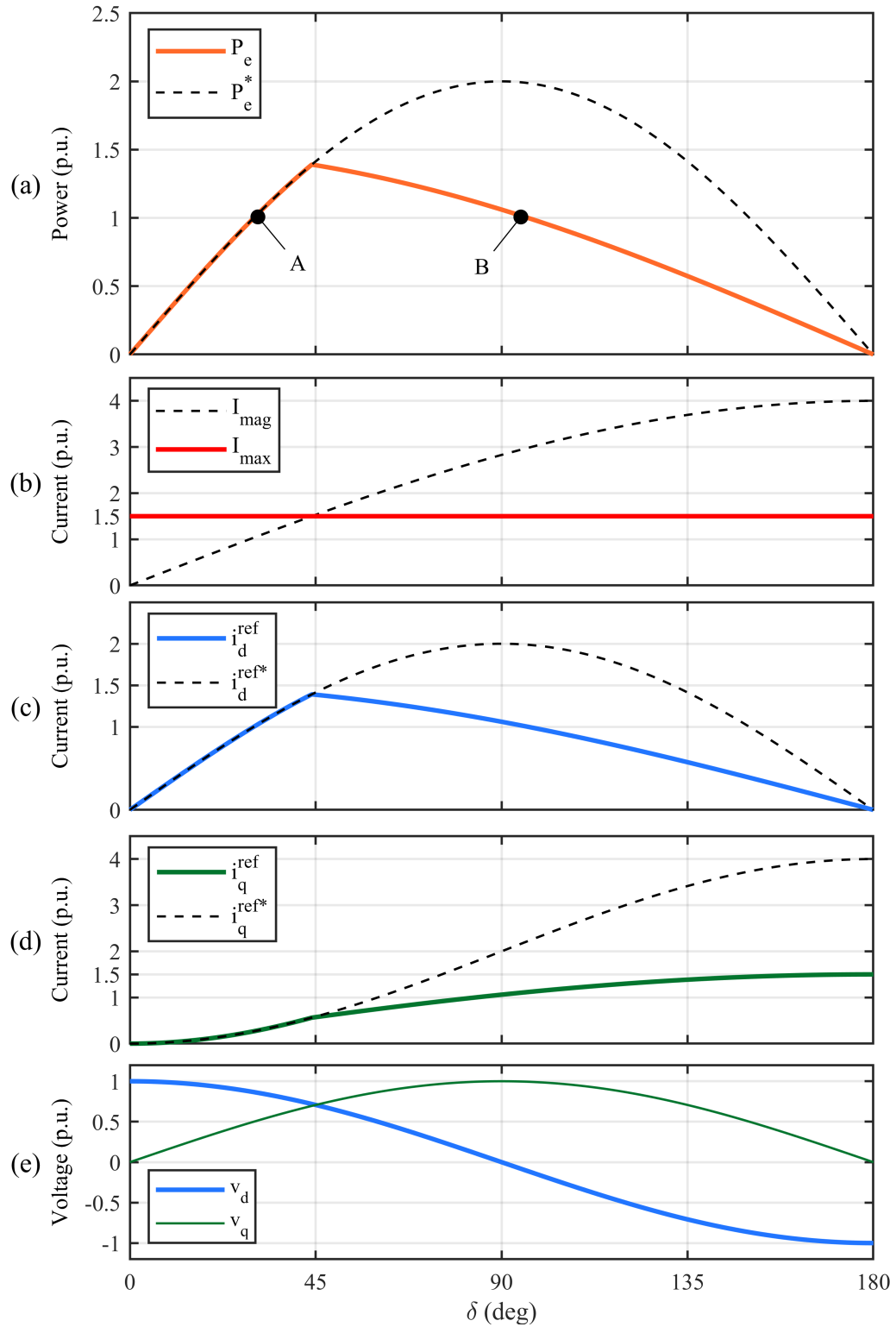


Figure 2. 8: Performance of the VSG utilizing the angle priority current limiting strategy (a) VSG power (b) VSG current (c) d -axis reference current (d) q -axis reference current (e) dq components of the grid voltages

2.4.2 d -axis Priority

If priority is given to the d -axis current (Figure 2.11(b)), i_d^{ref} is limited to the maximum current capacity I_{max} , and i_q^{ref} is limited such that the total current does not exceed the maximum current rating. If, during a large contingency, the magnitude of the dq -reference current lies outside the circle with radius I_{max} (black arrow), then the d -axis current is limited as (2.25). The maximum q -axis reference current is thus set as (2.26) and the output power is determined by (2.27) where i_d^{ref} and i_q^{ref} have the same signs as those of i_d^{ref*} and i_q^{ref*} , respectively [27], [41], [51]-[53], [92], [98]-[101]. Figure 2.13 shows how the d -axis priority current limiting strategy affects the $P - \delta$ characteristic of the VSG and its transient stability margins. Assuming that the VSG input power (virtual mechanical power P_m) is constant and equal to 1 p.u., which represents the worst case scenario, the VSG has two equilibrium points A and B. Small perturbation analysis shows that A is a stable equilibrium while B is an unstable one.

$$|i_d^{ref}| = \min(I_{max}, |i_d^{ref*}|) \quad (2.25)$$

$$|i_q^{ref}| = \min\left(\sqrt{(I_{max})^2 - (i_d^{ref})^2}, |i_q^{ref*}|\right) \quad (2.26)$$

$$P_e = \begin{cases} \frac{EV}{X_v} \sin\delta & , |i_d^{ref*}| < I_{max} \\ VI_{max} \cos\delta \operatorname{sign}(i_d^{ref*}) & , |i_d^{ref*}| \geq I_{max} \\ Vi_d^{ref*} \cos\delta + V\sqrt{I_{max}^2 - i_d^{ref*2}} \sin\delta & , O.W. \end{cases} \quad (2.27)$$

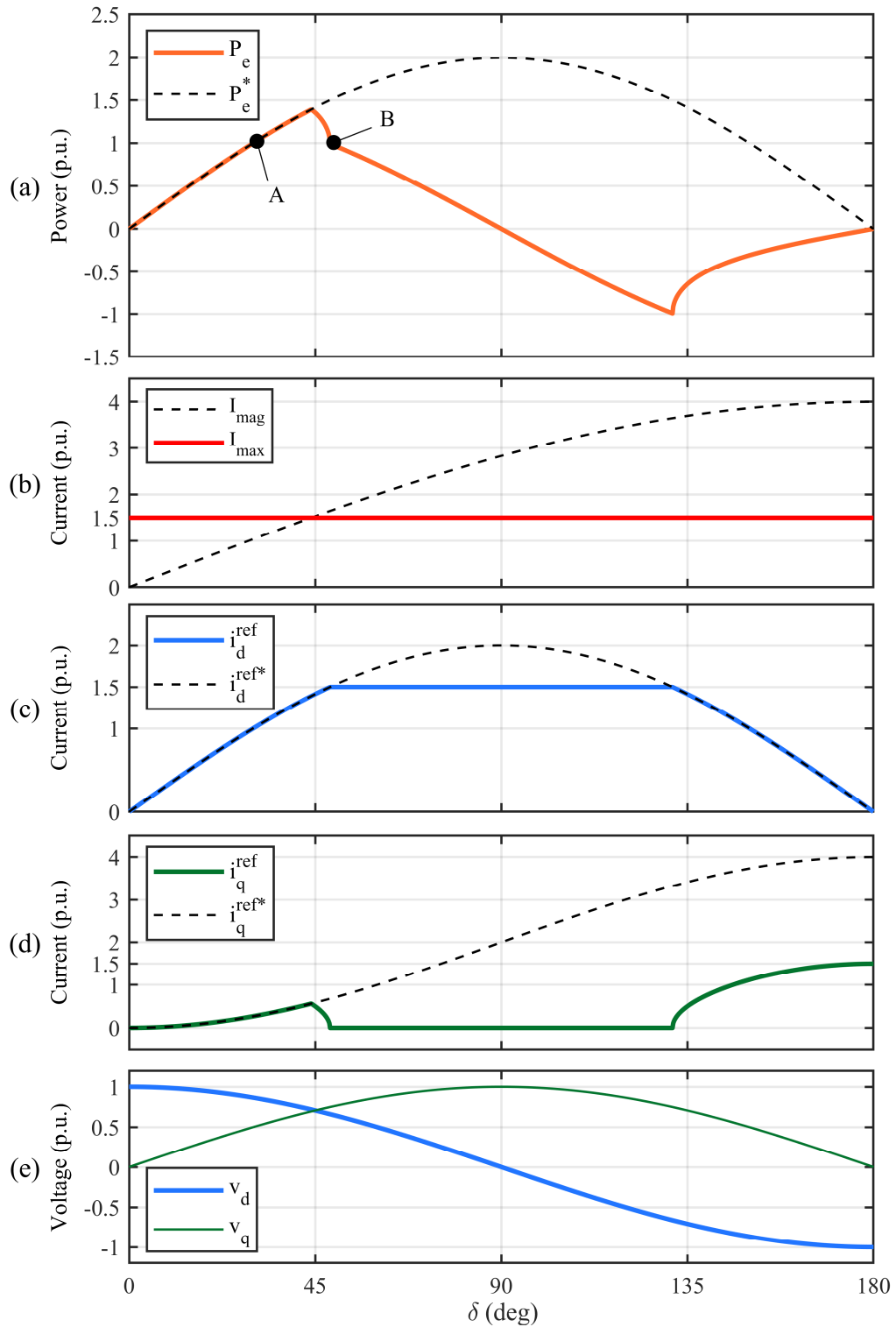


Figure 2. 9: Performance of the VSG utilizing the d -axis priority current limiting strategy (a) VSG power (b) VSG current (c) d -axis reference current (d) q -axis reference current (e) dq components of the grid voltages

2.4.3 q -axis priority

As shown in Figure 2.11(c), in this strategy i_q^{ref} is limited to the maximum current capacity I_{max} , and i_d^{ref} is limited such that the total current does not exceed the maximum rating. If, during a large disturbance, the current magnitude lies outside the circle with radius I_{max} , the q -axis current is limited according to (2.28). The maximum d -axis reference current is thus determined by (2.29) and the output current in the saturated mode is determined by (2.30) where i_d^{ref} and i_q^{ref} have the same signs as those of i_d^{ref*} and i_q^{ref*} , respectively [92], [102]-[106]. Figure 2.14 shows how the q -axis priority current limiting strategy affects the $P - \delta$ characteristic of the VSG and its transient stability margins. Assuming that the VSG input power (virtual mechanical power P_m) is constant and equal to 1 p.u., which represents the worst case scenario, the VSG has two equilibrium points A and B. Small perturbation analysis shows that A is a stable equilibrium while B is an unstable one.

$$|i_q^{ref}| = \min(I_{max}, |i_q^{ref*}|) \quad (2.28)$$

$$|i_d^{ref}| = \min\left(\sqrt{(I_{max})^2 - (i_q^{ref})^2}, |i_d^{ref*}|\right) \quad (2.29)$$

$$P_e = \begin{cases} \frac{EV}{x_v} \sin\delta & , |i_{dq}^{ref*}| < I_{max} \\ Vi_{max} \sin\delta & , i_q^{ref*} \geq I_{max} \\ V\sqrt{I_{max}^2 - i_q^{ref*2}} \cos\delta + Vi_q^{ref*} \sin\delta & , \text{O.W.} \end{cases} \quad (2.30)$$

According to Figure 2.11(a), Figure 2.12(a), and Figure 2.13(a), Although the angle priority current limiting strategy improves the transient stability of the VSG compared to d -axis priority to a greater extent, the q -axis priority brings even more stability to the VSG. Moreover, as the angle margin between the equilibrium points A and B increases, the VSG transient stability improves.

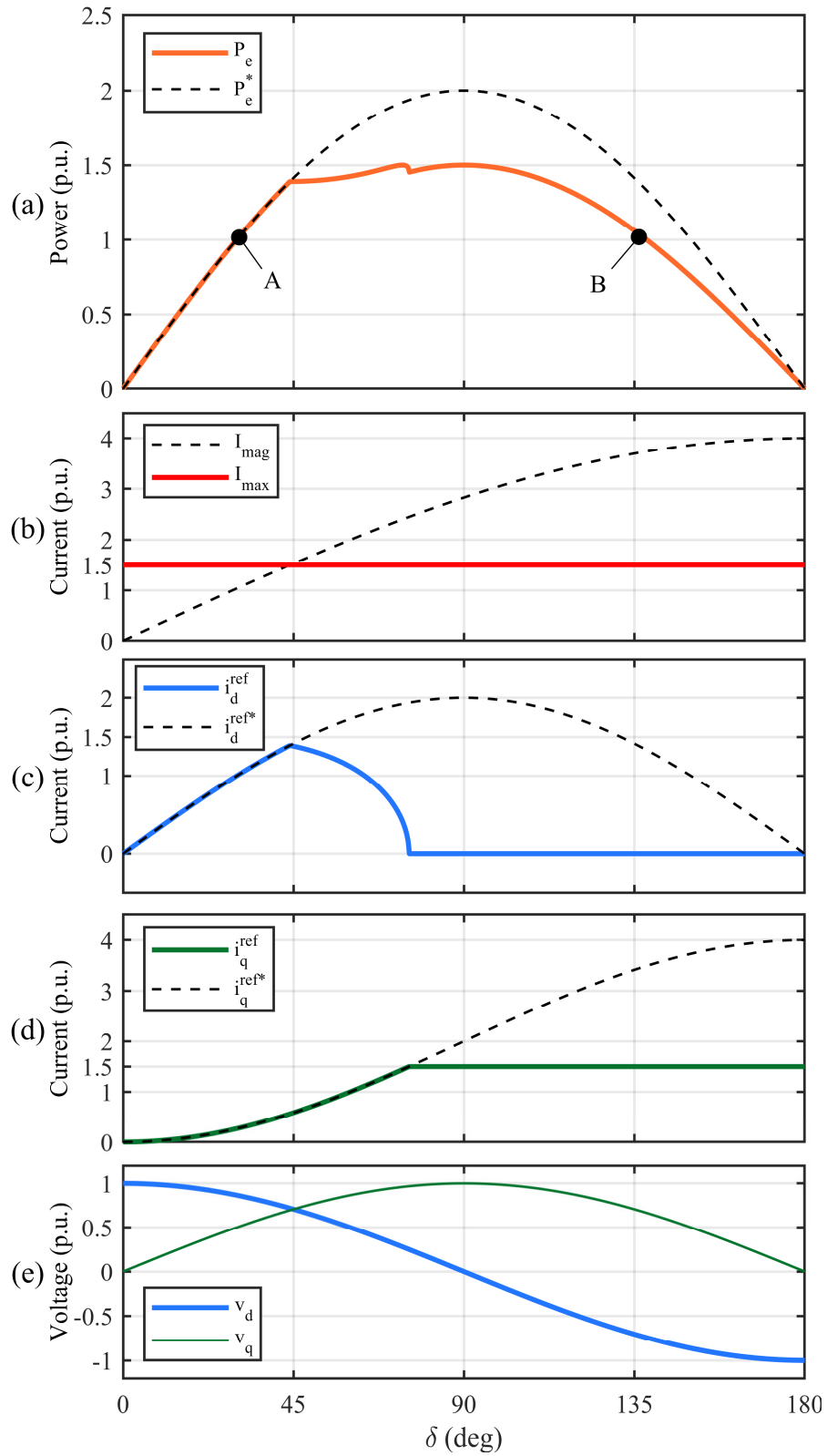


Figure 2. 10: Performance of the VSG utilizing the q -axis priority current limiting strategy (a) VSG power (b) VSG current (c) d -axis reference current (d) q -axis reference current (e) dq components of the grid voltages

2.5 Performance Evaluation

In this section, the current limiting strategies discussed in the previous parts are investigated and compared through detailed time-domain simulation studies in the PSCAD software. The VSG response to various disturbances is investigated and its transient stability under various fault scenarios is evaluated by analyzing the CCT. In addition, the impacts of virtual impedance on the transient stability is investigated.

2.5.1 Validation of VSG Output Power in Saturation Mode

In order to validate the analytical studies of the part 2.4, the VSG performance under various fault scenarios is investigated. To consider the effects of short circuit capacity on the transient stability of the VSG, the VSG is moved to different nodes in the study systems and the fault are applied to different locations.

It is assumed that the VSG is connected to the Node N1 in the study system of Figure 2.15, and a three-phase solid fault (F1 in Figure 2.15) takes place at the same location. To obtain the $P - \delta$ characteristics, a small virtual damping is intentionally chosen for the VSG. Figure 2.16 compares the performance of the dq priority current limiting strategy on the transient stability of the VSG under the three-phase to ground fault (F1) in PSCAD with the theoretical results plotted using MATLAB. It can be observed that the simulation matches with theory.

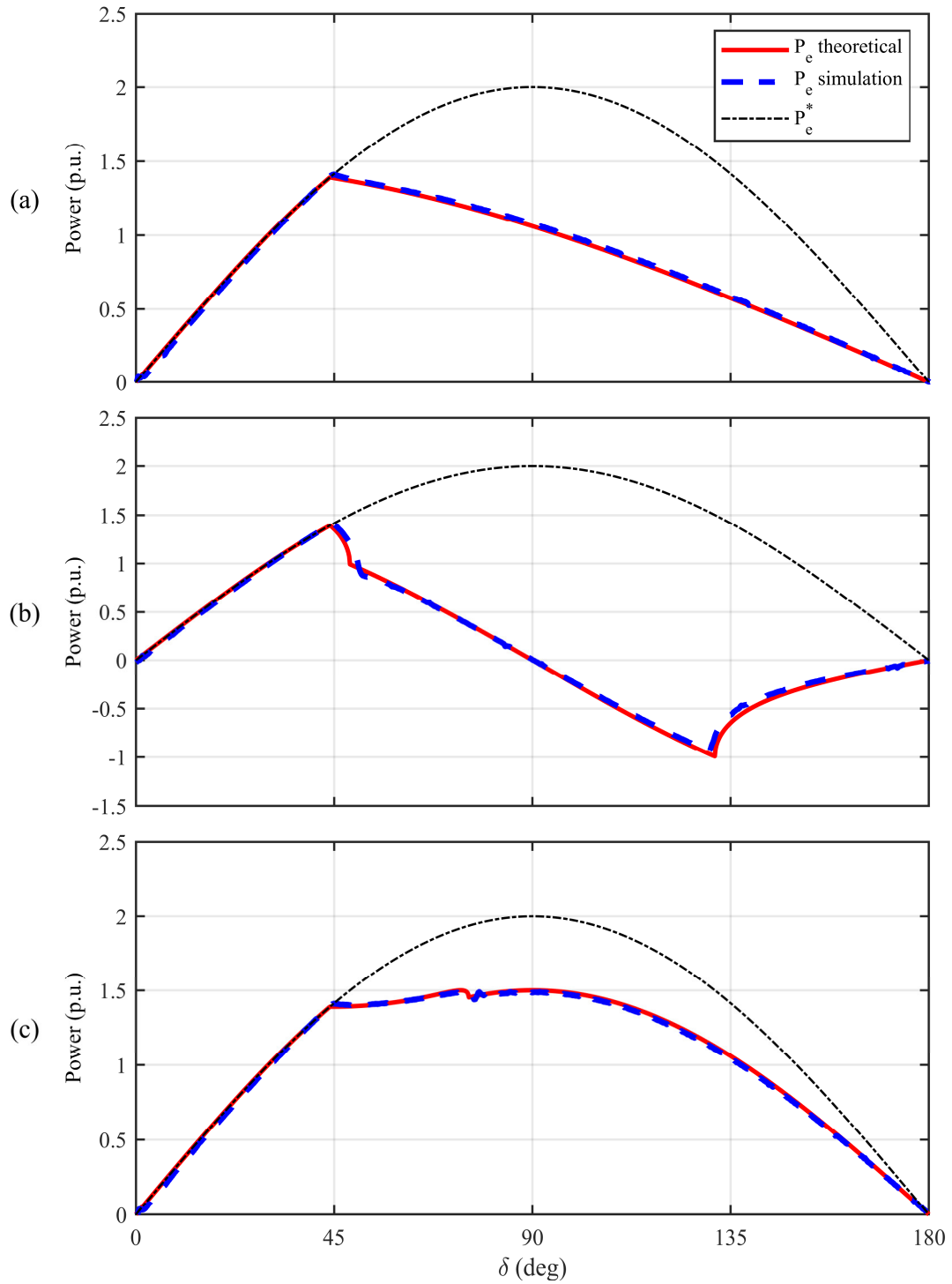


Figure 2. 12: Comparison of the VSG P - δ characteristics obtained based on theoretical analysis and time-domain simulation (a) angle priority (b) d -axis priority (c) q -axis priority

2.5.2 Comparison of Current Limiting Strategies

Figures 2.17, 2.18 and 2.19 show the performance of the VSG under a solid three-phase to the ground fault (F1 in Figure 2.15) based on the angle priority, d -axis priority and q -axis priority current limiting strategies, respectively. As shown in Figures 2.17, 2.18 and 2.19, before the disturbance is applied at $t = 0.5$ s, the system is in steady-state, and the VSG is at the equilibrium $\delta = 30^\circ$ and $\omega = 377$ rad/s. The damping is chosen such that the VSG has overshoot no more than 10%, i.e., based on the results of the eigenvalue analysis in part 2.3. The fault resistance is assumed to be zero and the fault lasts for 350 ms. The fault durations this study is considered to be significantly long. The fault clearing time in a practical distribution system is typically shorter. However, this long fault duration is used to represent the worst-case scenario.

During the fault, since the output power of the VSG is zero, the VSG starts to accelerate which leads to increased δ and ω . Once the fault is cleared at $t = 0.85$ s, the obtained results show that the VSG utilizing the q -axis priority current limiting strategy remains stable and returns to its equilibrium (Figure 2.19), while the other two strategies start accelerating and becoming unstable (Figures 2.17 and 2.18).

Figure 2.20 compares the $\omega - \delta$ trajectory of the VSG after this fault scenario F1 under different current limiting strategies. As shown in Figure 2.20, once the fault is cleared, the ω and δ of the VSGs adopting the angle priority (black curve) and the d -axis priority (blue curve) keep increasing along the saturated virtual power angle curve and the VSG starts accelerating and cannot maintain synchronism with the grid, leading to the transient instability. After a current polarity reversal, they return to stable operation at a new equilibrium around $\delta = 390^\circ$ and $\omega = 377$ rad/s. However, the q -axis priority, after fault clearance, starts decelerating and returns to its previous equilibrium without any current polarity reversal.

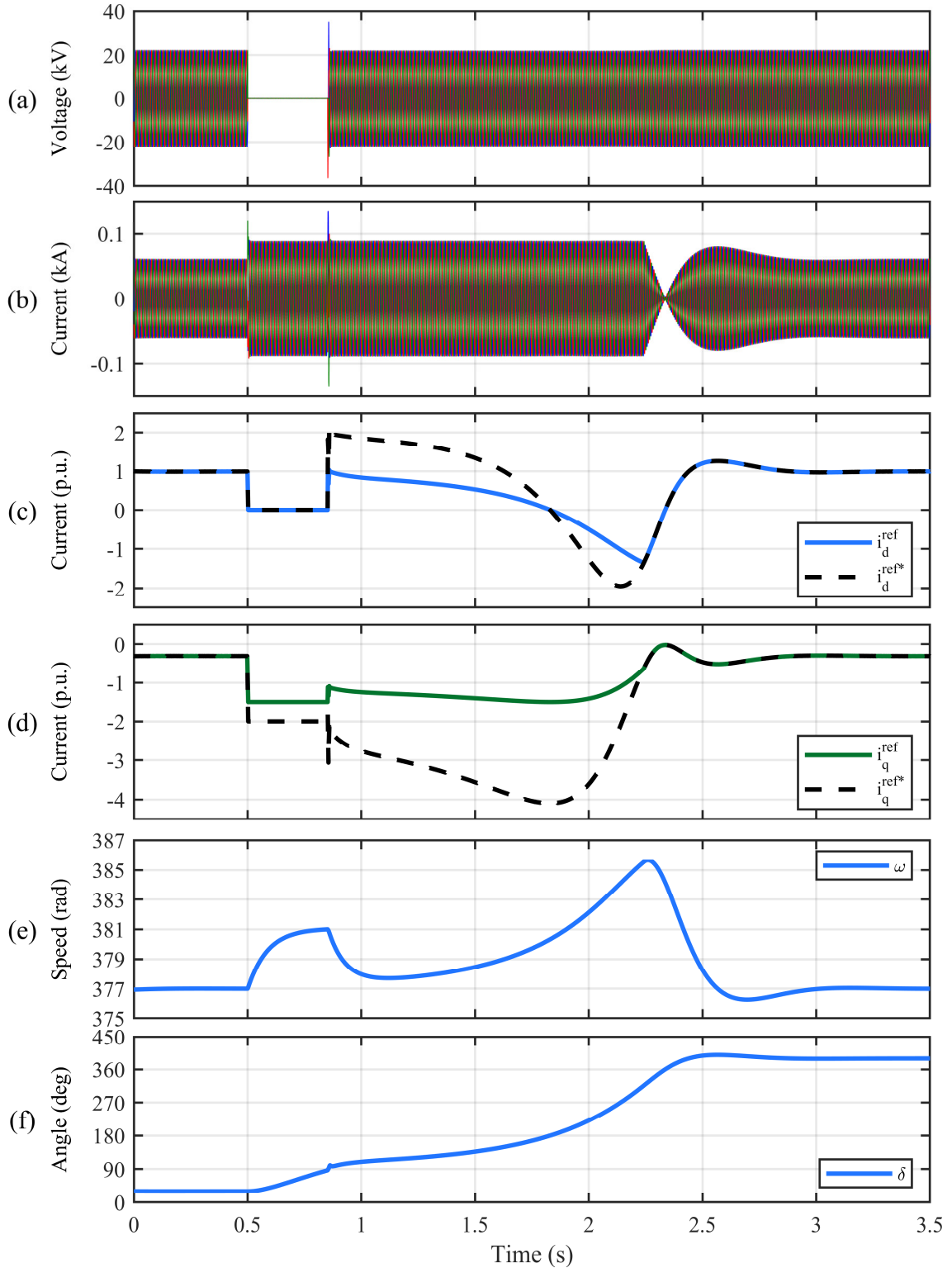


Figure 2. 13: Performance of the VSG based on the angle priority (a) VSG terminal voltages (at 27.6 kV-side of transformer) (b) VSG terminal currents (at 27.6 kV-side of transformer) (c) d-axis reference currents (d) q-axis reference currents (e) VSG angular speed (f) power angle

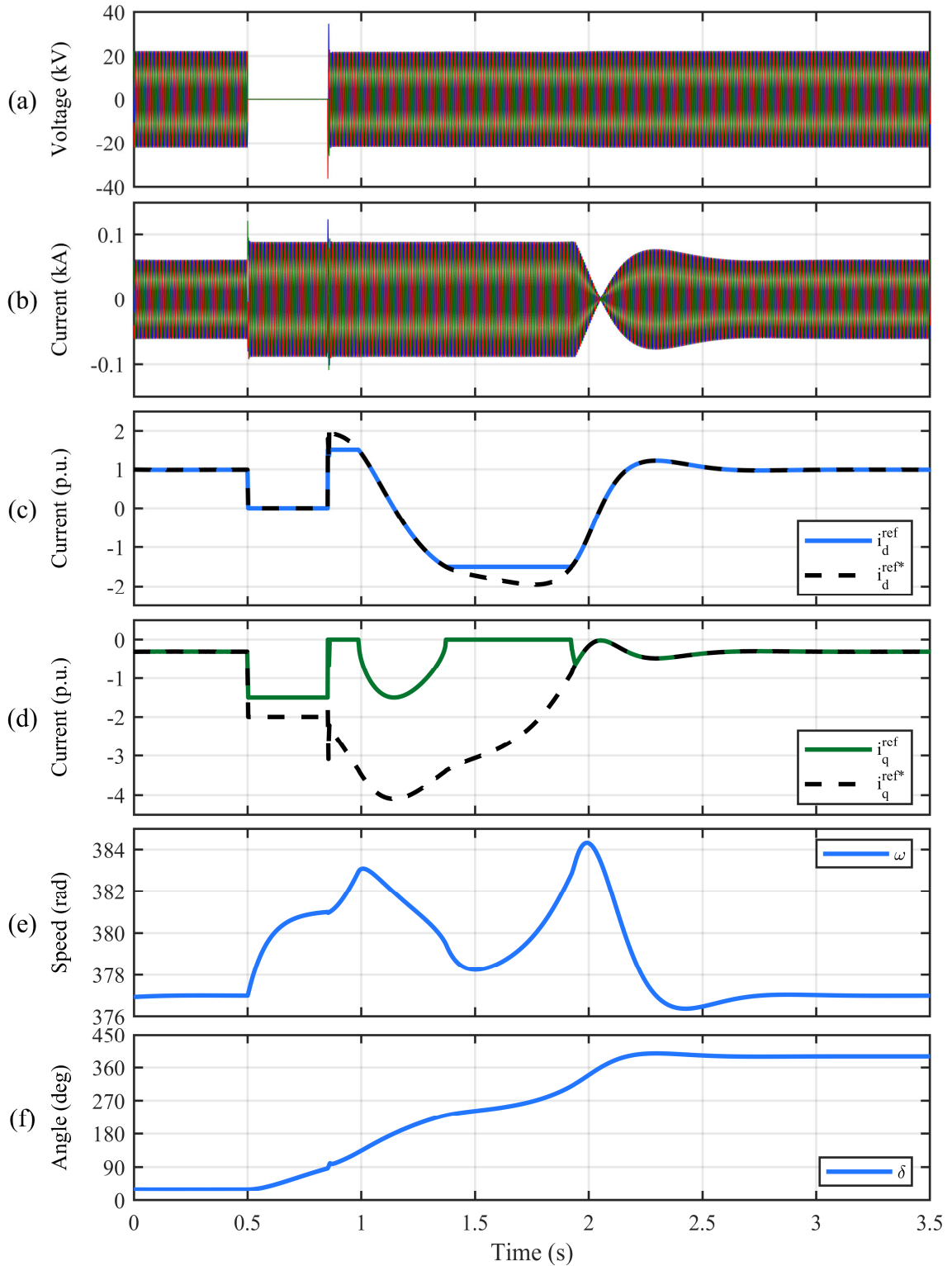


Figure 2. 14: Performance of the VSG based on the d -axis priority (a) VSG terminal voltages (at 27.6kV-side of transformer) (b) VSG terminal currents (at 27.6 kV-side of transformer) (c) d -axis reference currents (d) q -axis reference currents (e) VSG angular speed (f) power angle

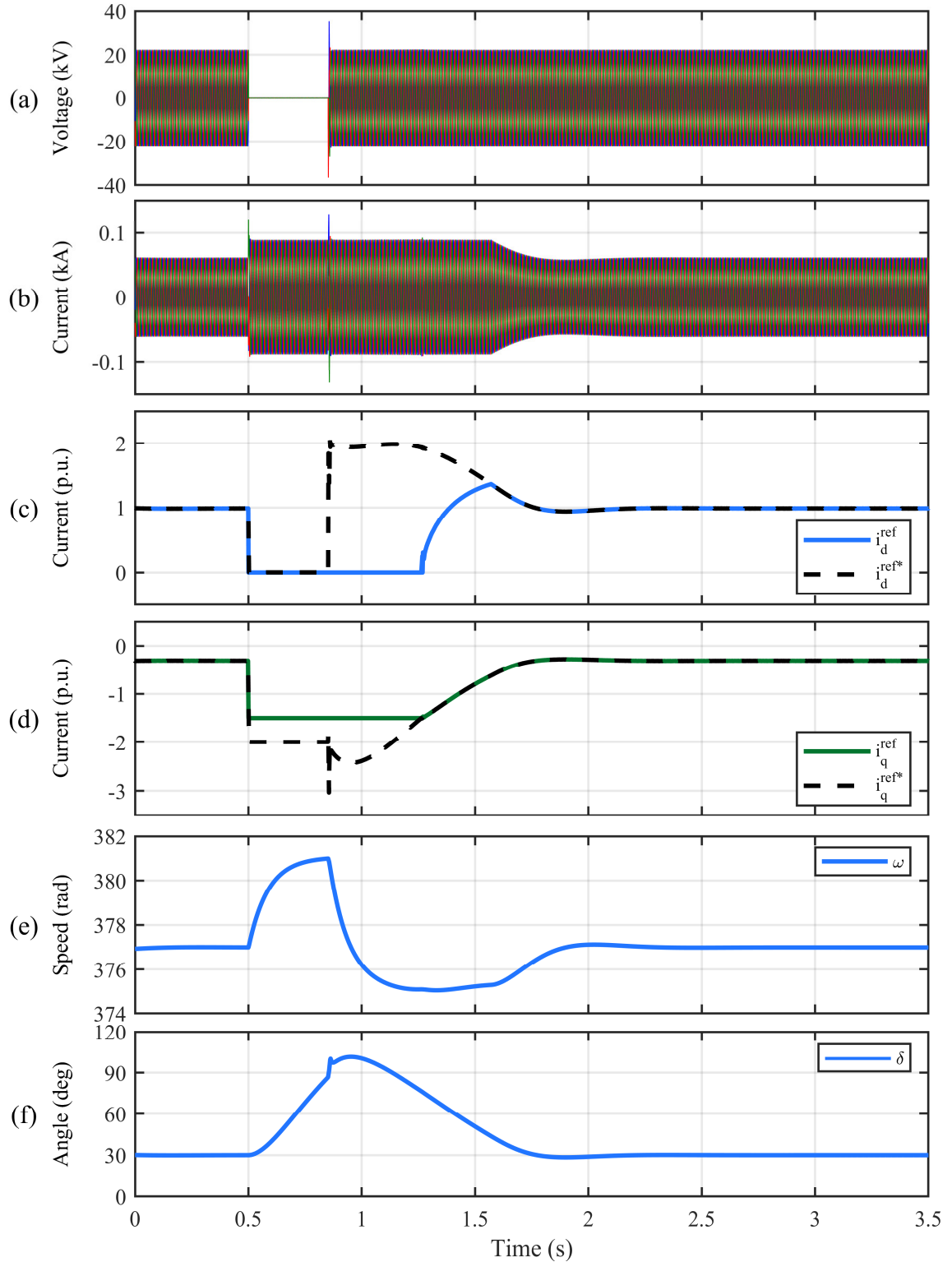


Figure 2. 15: Performance of the q -axis priority (a) VSG terminal voltages (at 27.6kV-side of transformer) (b) VSG terminal currents (at 27.6 kV-side of transformer) (c) d-axis reference currents (d) q-axis reference currents (e) VSG angular speed (f) power angle

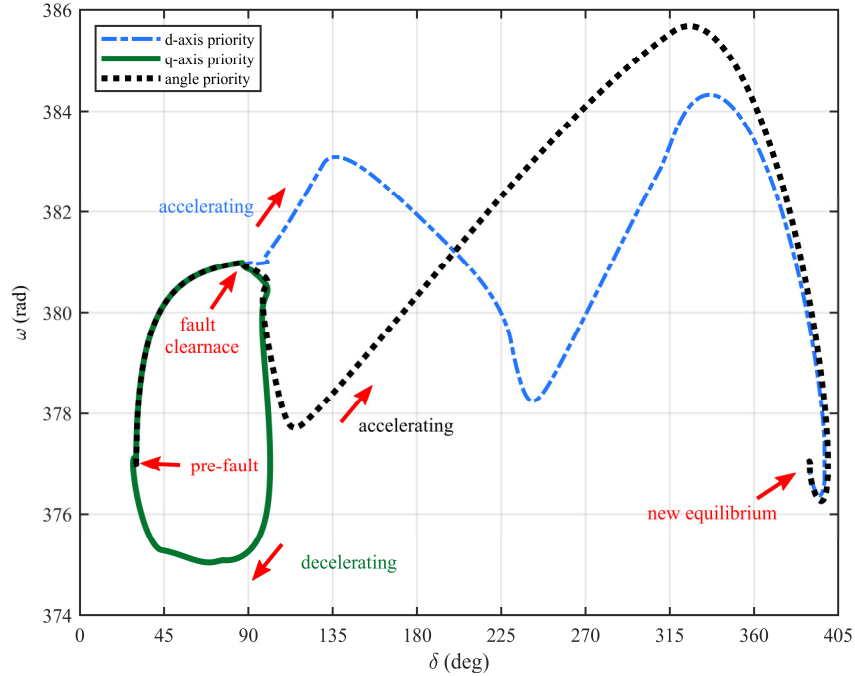


Figure 2. 16: The operating point trajectory of VSG subjected to a three-phase fault at F1 under different current limiting strategies

The most severe fault (three-phase solid fault) is applied to different locations (Faults $F1-F7$ in Figure 2.15), and the VSG is assumed to be connected to different nodes (node $N1, N5, N10, N13, N16, N17$ in Figure 2.15). The current limiting strategies are compared based on their impacts on the obtained CCTs. The results are shown in Table 2.2.

As shown in Table 2.2, 49 different scenarios are investigated. The first row of the Table 2.2 verifies the results illustrated in Figures 2.17-2.20 and indicates that the fault duration of 350 ms is less than the CCT of the q -axis priority current limiting strategy and more than those of the other two strategies. According to the results, the different current limiting strategies lead to different CCTs and the q -axis priority current limiting is the best strategy from the VSG transient stability perspective. In other words, if the q -axis reference priority is adopted, the protection systems have more time to clear the fault prior to VSG instability.

Table 2. 2 Comparison of the different current limiting strategies

VSG location	Fault location	CCT (ms)		
		<i>d</i> -axis priority	<i>q</i> -axis priority	angle priority
N1	F1	112.5	475	301
	F2	129.6	570	362.5
	F3	226	1260	815
	F4	-	-	-
	F5	-	-	-
	F6	-	-	-
	F7	-	-	-
N5	F1	112.98	474	301
	F2	112.96	473	298
	F3	187	940	610
	F4	477	-	-
	F5	-	-	-
	F6	-	-	-
	F7	-	-	-
N8	F1	112.97	475	299
	F2	112.96	474	299
	F3	112.9	473	298
	F4	199	1325	810
	F5	307	2950	1690
	F6	312.5	2535	1440
	F7	440	4850	2450
N10	F1	118	471	296
	F2	117	471	293
	F3	115	465	293
	F4	115	465	290
	F5	160	660	422.5
	F6	160	645	415
	F7	193	770	505
N16	F1	120.5	470	295
	F2	121	470	293
	F3	121	470	293
	F4	121	467.5	288
	F5	121	462.5	285
	F6	168	625	415
	F7	201	778	510
N17	F1	120.5	477.5	299
	F2	120.5	477.5	299
	F3	120.5	475	297
	F4	120.5	475	295
	F5	165	675	430
	F6	118	450	292
	F7	151.5	605	385
N13	F1	124.5	479	301
	F2	120.5	479	299
	F3	120.5	760	298
	F4	120.5	474	296
	F5	167	675	435
	F6	132	510	315
	F7	121	465	290

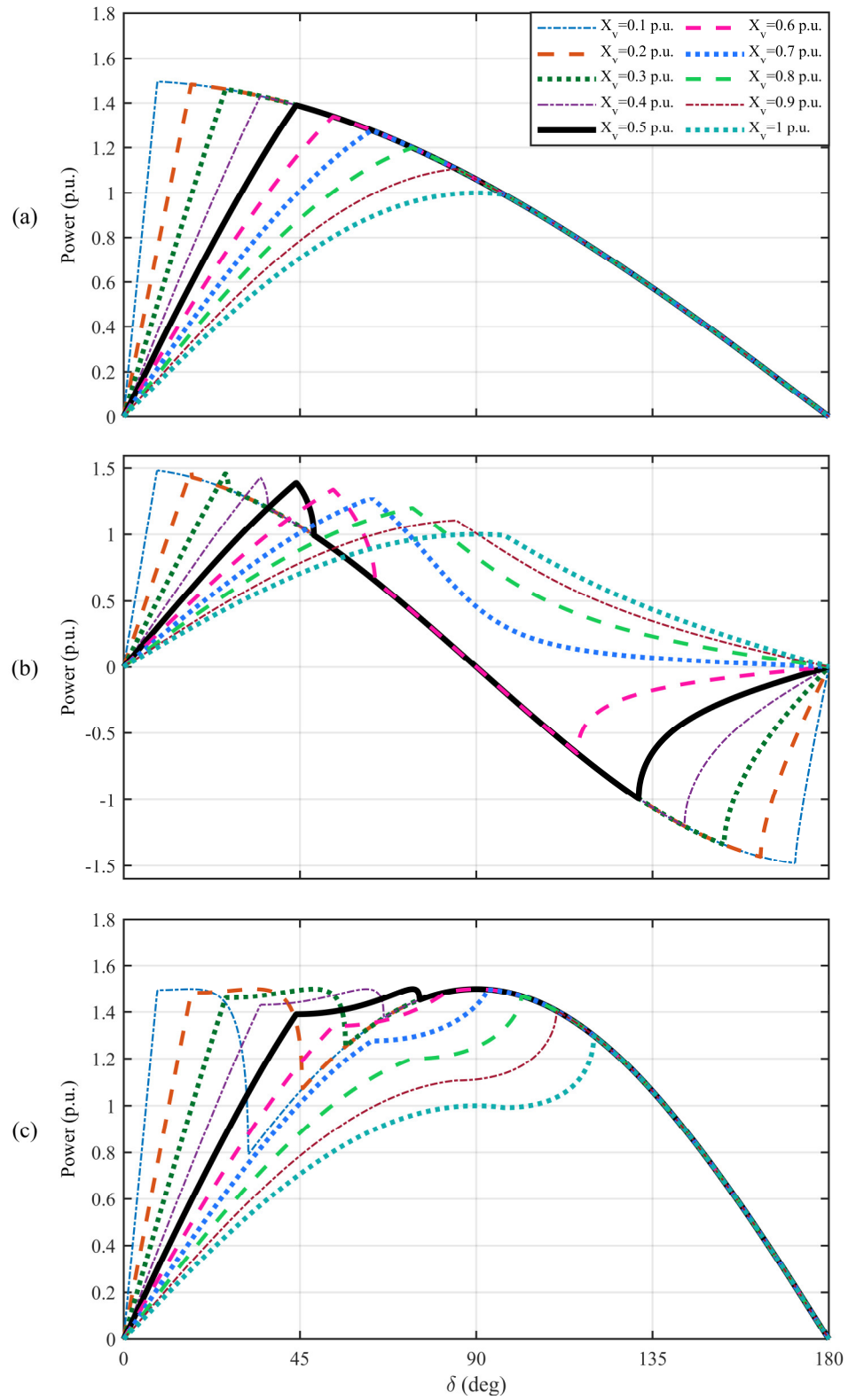


Figure 2.17: Impacts of X_v on transient stability (a) angle priority (b) d-axis priority (c) q-axis priority

2.5.3 The Effect of Virtual Impedance on Transient stability

According to equation (2.12), the poles are affected by D_p , and J and X_v . The impacts of damping factor and moment of inertia have been investigated. The impacts of virtual reactance on transient stability is investigated in this part. Figure 2.21 illustrates the influence of virtual impedance on the VSG $P - \delta$ characteristic under different current limiting strategies. The study results indicate that, for X_v values in typical range (from 0.1 p.u. to 1 p.u.), regardless of the virtual reactance values, the q -axis current reference priority leads to more VSG transient stability margin as compared to the other two strategies.

2.6 Conclusion

In this chapter, the VSG control systems is introduced. To verify small signal stability and ensure desirable dynamic response of the VSG to disturbances, the appropriate values of the VSG parameters are determined based on eigenvalue analysis. Subsequently, different current limiting strategies theoretically and numerically investigated in terms of their impacts on the transient stability of the VSG after a large disturbance by calculating the CCT after a fault. An extensive simulation is carried out to verify the validity of theoretical analysis and the effectiveness of current limiting strategies on transient stability of the VSG under various disturbances. The study results indicate that:

- Smaller H value leads to a more desirable dynamic response, i.e., smaller overshoot and settling time. However, reducing the inertia is counterproductive since the main goal of using a VSG is to emulate inertia.
- Increasing damping factor causes the peak time increases, while the overshoot and settling time decrease. Therefore, a larger D_p result in a better output active power dynamic performance with lower oscillations but slower response.
- Although the angle priority improves the transient stability of the VSG compared to d -axis priority to a greater extent, the q -axis priority brings even more stability to the VSG.
- smaller virtual impedance increases the VSG critical clearing time and improves the transient stability of the system.

Chapter 3

3 Impacts of Damping on the VSG Transient Stability

3.1 Introduction

In this chapter, a theoretical analysis is performed to compare the acceleration behavior of the VSG with negligible damping (similar to a SG), the VSG with small damping and the VSG with large damping, under fault disturbances, to evaluate the effects of different damping values on the critical clearing time of faults. In addition, detailed simulation studies are carried out to verify the validity of theoretical analysis.

Subsequently, an adaptive damping control system for enhanced transient stability of the VSG is proposed and verified through numerous fault studies. The effectiveness of the proposed adaptive damping control system is verified through time-domain simulation studies conducted in the PSCAD software environment using a realistic study system.

3.2 Theoretical Analysis

In a synchronous generator connected to grid, when a fault happens, the power delivering capacity of the machine suddenly reduces. Thus, the input power is greater than output power. Since the SG has a negligible damping, this imbalance causes acceleration of the rotor and force it to run above synchronous speed and the δ starts to rise. The power angle, δ increases exponentially, as described by (3.1) [107].

$$\delta(t) = \frac{\omega_s P_{in}}{4H} t^2 + \delta_0 \quad (3.1)$$

In a VSG, the virtual damping limits the increase in ω and delays instability under fault condition. If the damping factor is large, the acceleration will be damped very fast, whereas if the damping factor is small, the VSG will accelerate with higher rate of change of frequency and the acceleration will be stopped slowly. Thus, the VSG remains stable

damping. In other words, large damping factor leads to shorter amount of acceleration time and vice versa.

3.3 Performance Evaluation

To validate the abovementioned analysis, the acceleration behavior of SG and the VSG under different damping conditions are investigated in PSCAD. A three-phase-to-ground fault with zero resistance (the fault in Figure 3.2) takes place at the same location as VSG (node N1 in Figure 3.2). The detailed VSG parameters are shown in Table 2.1. As demonstrated in Chapter 2, the q -axis priority current limiting strategy improves the transient stability of the VSG more than the other two current limiting strategies. Therefore, this current limiting priority is utilized for the rest of this chapter. In this chapter, the small damping factor is the value determined using eigenvalue analysis in Chapter 2.

Figure 3.3 illustrates the performance of the VSG with negligible damping (similar to a SG) under the aforementioned fault scenario. As shown in Figure 3.3, before the disturbance is applied, the VSG is in the steady-state, and the system is at the equilibrium $\delta = 30^\circ$ and $\omega = 377 \text{ rad/s}$. A three-phase solid fault occurs at $t = 0.5 \text{ s}$ and the fault duration is 500 ms. The fault durations this study is considered to be significantly long. The fault clearing time in a practical distribution system is typically shorter. However, this long fault duration is used to represent the worst-case scenario.

During the fault, since the output power of the VSG is zero, the VSG starts to accelerate which causes the δ and ω to increase. Once the fault is cleared at $t = 1 \text{ s}$, since the damping factor of the VSG is negligible, the δ and ω keep increasing and the VSG never returns to stable operation.

The $\omega - \delta$ characteristics of the VSG is shown in Figure 3.4. As shown in Figure 3.4, once the fault is cleared, the ω and δ keep increasing and the VSG cannot maintain synchronism with the grid, leading to the transient instability.

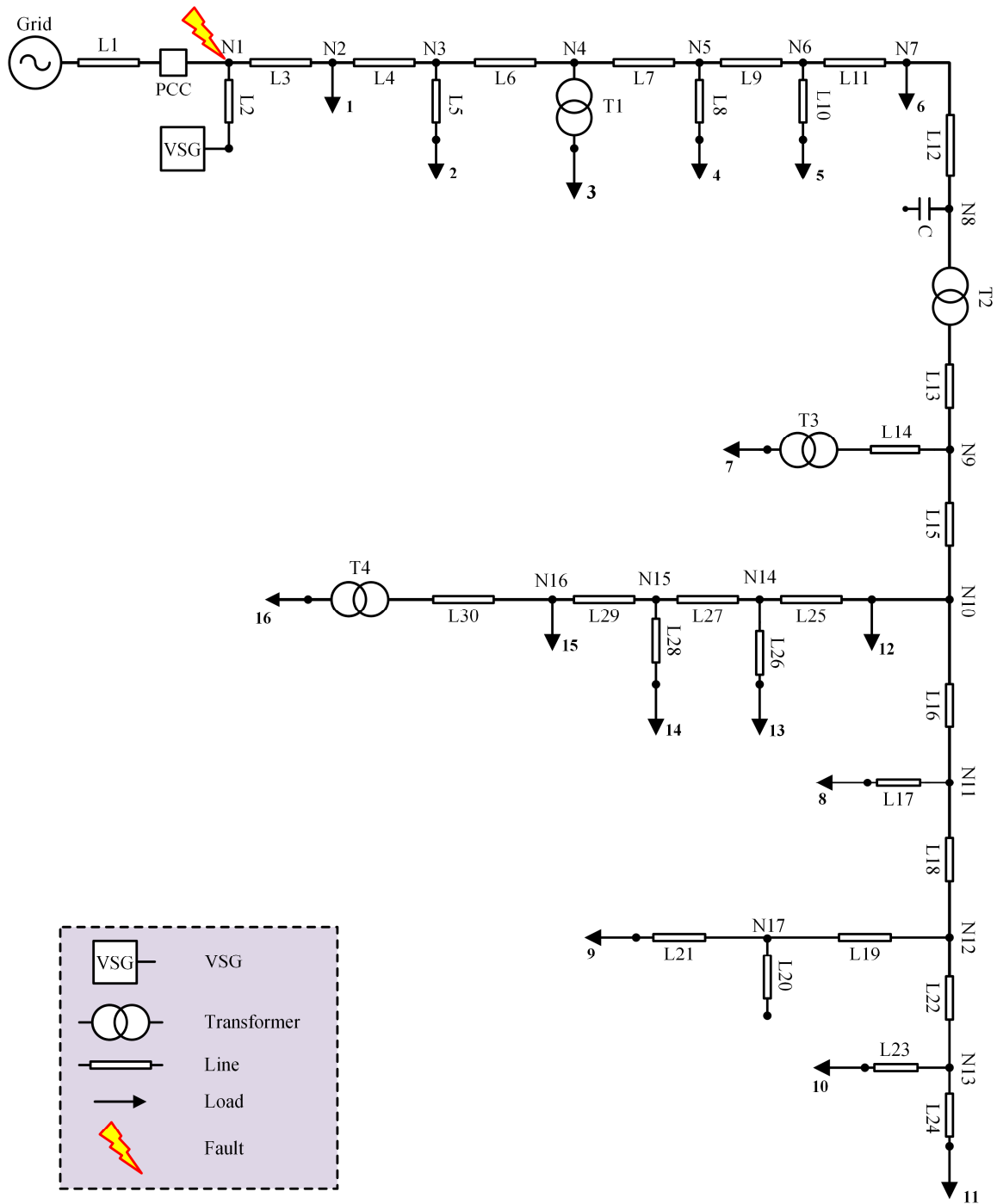


Figure 3. 2: Single-line diagram of the study system with the location of fault

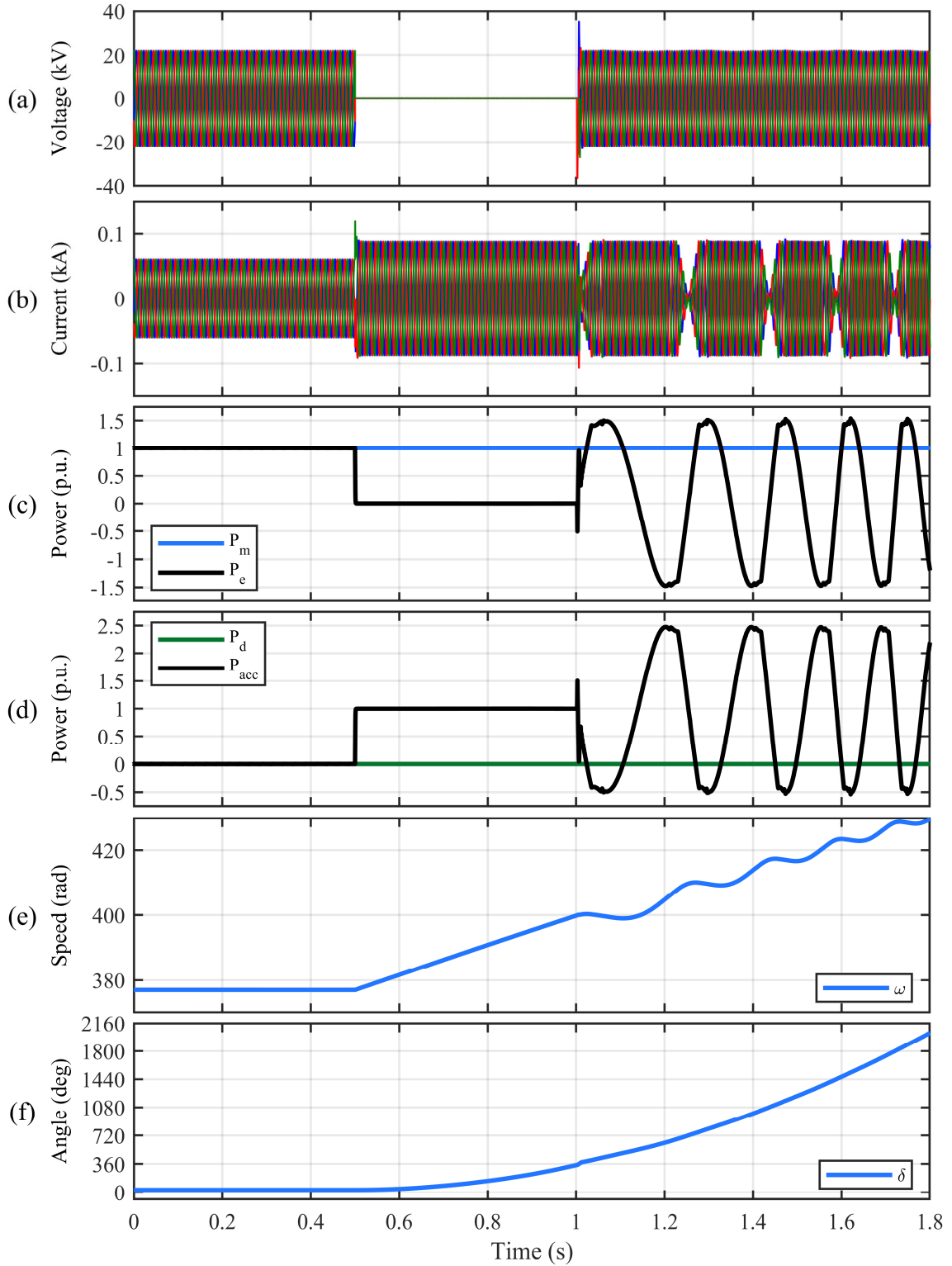


Figure 3.3: Performance of the VSG with negligible damping under a three-phase fault at node N1 (a) VSG terminal voltages at 27.6kV-side of transformer (b) VSG terminal currents at 27.6kV-side of transformer (c) mechanical and electrical powers (d) acceleration and damping powers (e) VSG angular speed (f) power angle

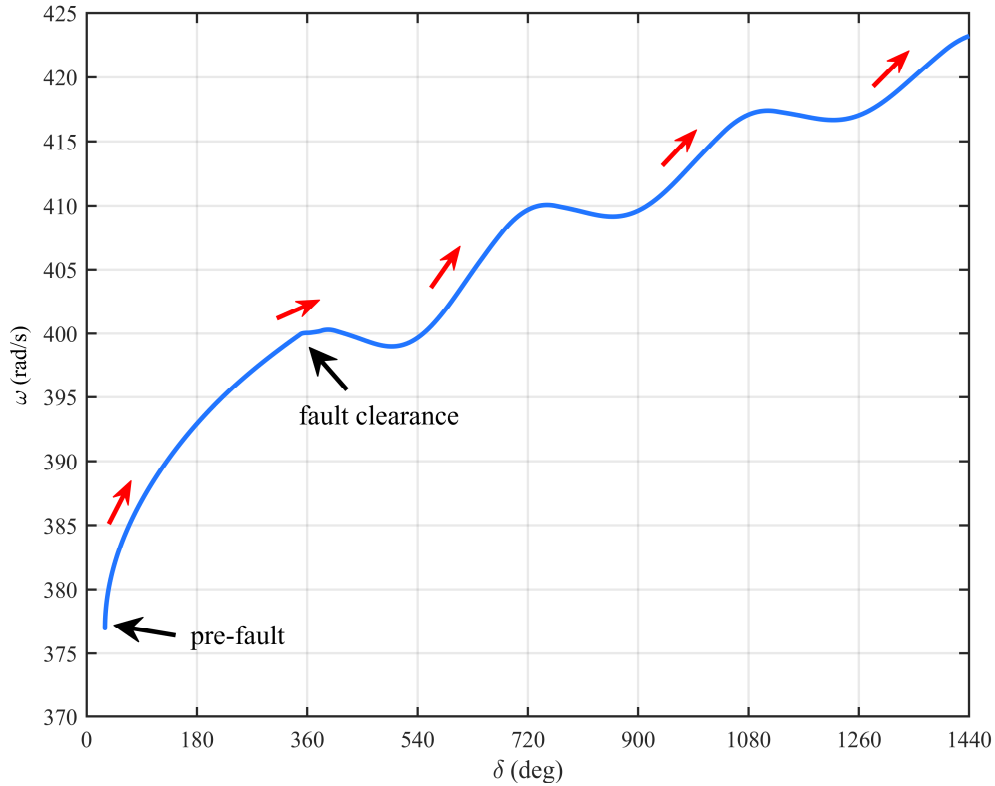


Figure 3. 4: Operating point (state transition) trajectory of the VSG with negligible damping, subjected to a three-phase fault

Figure 3.5 illustrates the performance of the VSG with small damping factor under a three-phase fault at node N1. As shown in Figure 3.5, before the disturbance is applied at $t = 0.5 \text{ s}$, the system is in steady-state, and the VSG is at the equilibrium $\delta = 30^\circ$ and $\omega = 377 \text{ rad/s}$. The fault resistance is assumed to be zero and the fault lasts for 500 ms.

During the fault, since the output power of the VSG is zero, the VSG starts to accelerate which causes the δ and ω to increase. However, due to the virtual damping in the VSG, the acceleration stops in around 300 ms. Once the fault is cleared at $t = 1 \text{ s}$, the obtained results show that the VSG starts to accelerate which leads to increase δ and ω and after current polarity reversal, the VSG reaches new equilibrium $\delta = 390^\circ$ and $\omega = 377 \text{ rad/s}$ and becomes stable.

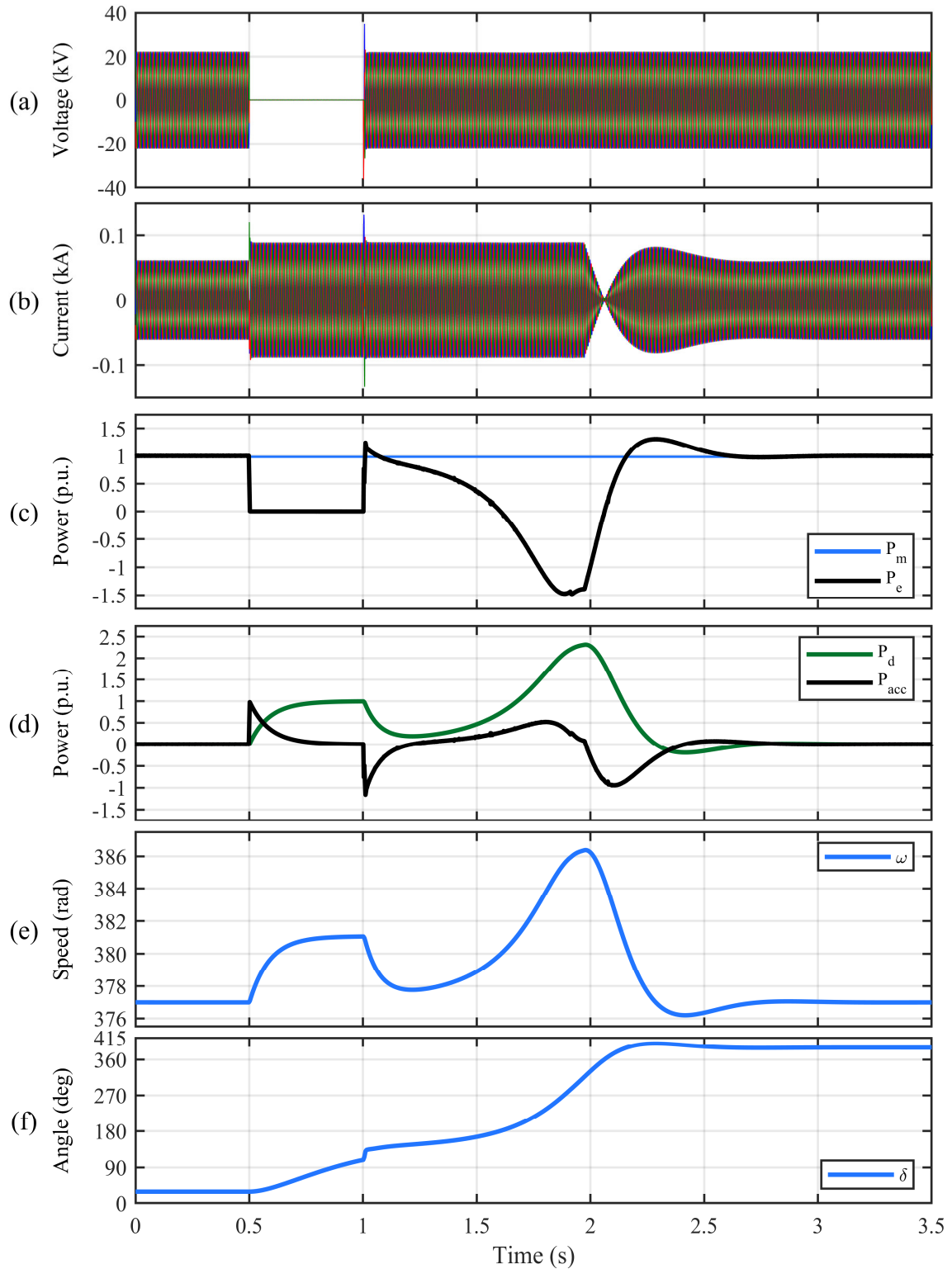


Figure 3. 5: Performance of the VSG with small damping under a three-phase fault at node N1 (a) VSG terminal voltages at 27.6kV-side of transformer (b) VSG terminal currents at 27.6kV-side of transformer (c) mechanical and electrical powers (d) acceleration and damping powers (e) VSG angular speed (f) power angle

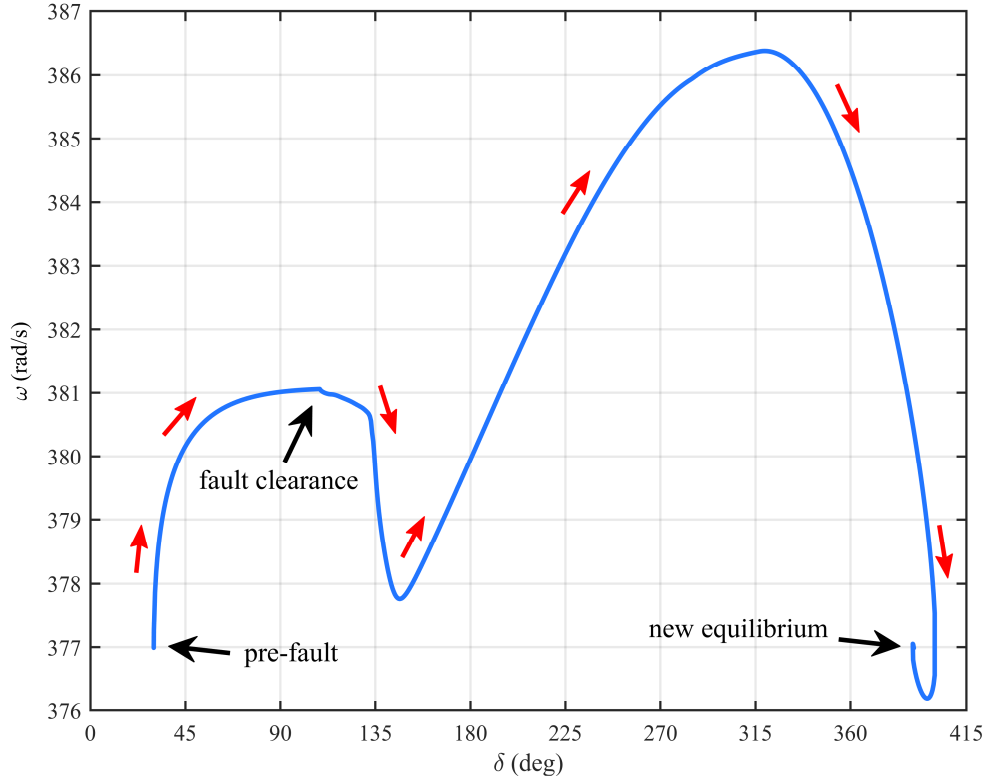


Figure 3. 6: Operating point (state transition) trajectory of the VSG with small damping, subjected to a three-phase fault

Figure 3.6 shows the $\omega - \delta$ trajectory of the VSG with small damping factor under aforementioned fault scenario. As shown in Figure 3.6, once the fault is cleared, the ω and δ keep increasing and the VSG cannot maintain synchronism with the grid, leading to the transient instability. After current polarity reversal, the VSG returns to the stable mode at a new equilibrium point around $\delta = 390^\circ$ and $\omega = 377 \text{ rad/s}$.

According to (3.2), to stop the VSG from acceleration during the fault and enable FRT according to the existing grid codes, the VSG acceleration power must be equal to zero.

$$\frac{P_{acc}}{J\omega} = \frac{P_m - P_e - D_p \Delta\omega}{J\omega} = \frac{d\omega}{dt} = 0 \quad (3.2)$$

During the fault the VSG output power P_e is equal to zero. Therefore, to prevent the VSG from becoming unstable, the damping factor must be:

$$D_p \geq \frac{P_m}{\Delta\omega} \quad (3.3)$$

The minimum damping factor value which keeps the VSG stable during and after the fault and bring it back to stable mode can be calculated as follows. According to (2.10), the δ_0 can be calculated as:

$$\delta_0 = \sin^{-1}\left(\frac{P_e X_v}{EV}\right) \quad (3.4)$$

The critical clearing angle (δ_{cr}) is equal 120° according to Figure 2. 21 and $\Delta\omega$ can be calculated by (3.5).

$$\Delta\omega = \frac{(\delta_{cr} - \delta_0)}{t_c} \quad (3.5)$$

By substitution (3.4) into (3.5), (3.3) becomes:

$$D_p \geq \frac{P_m t_c}{\delta_{cr} - \sin^{-1}\left(\frac{P_e X}{EU}\right)} \quad (3.6)$$

The equation (3.6) in per-unit value can be written as:

$$D_p \geq \frac{\omega_0 t_c}{\delta_{cr} - \sin^{-1}\left(\frac{P_e X}{EU}\right)} \quad (3.7)$$

As an example, assume $P_e = 1$ p.u. and $t_c = 1$ s. Then, $\delta_0 = 30^\circ$ and $\delta_{cr} = 120^\circ$. Therefore, $D_p \geq 240$ p. u.. Figure 3.8 illustrates the performance of the VSG with large damping factor ($D_p = 240$ p. u.) under a three-phase fault at node *NI*. As shown in Figure 3.7, before the disturbance is applied at $t = 0.5$ s, the system is in steady-state, and the VSG is at the equilibrium $\delta = 30^\circ$ and $\omega = 377$ rad/s. The fault resistance is assumed to be zero and the fault lasts for 500 ms.

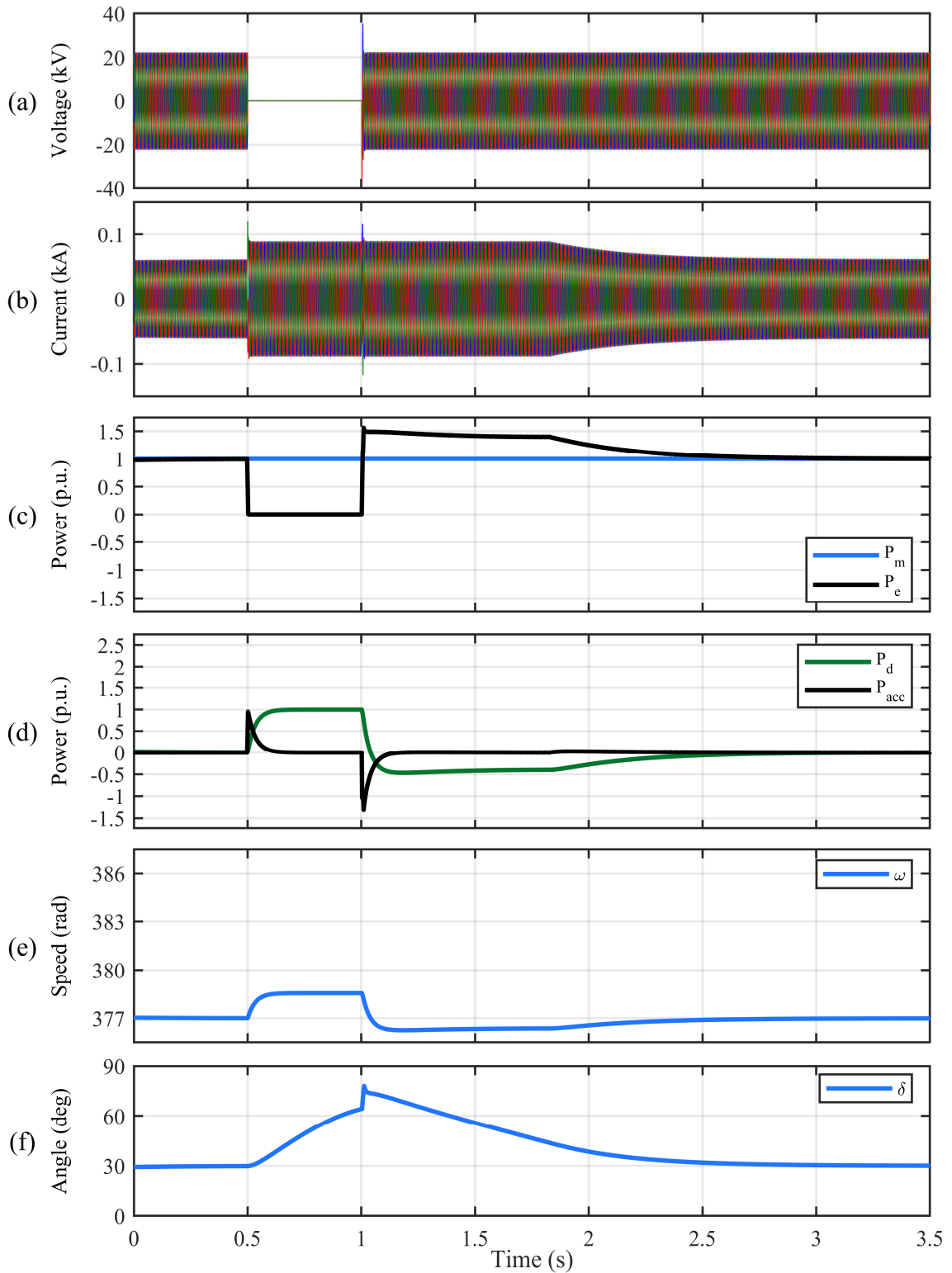


Figure 3. 7: Performance of the VSG with large damping under a three-phase fault at node NI (a) VSG terminal voltages at 27.6 kV-side of transformer (b) VSG terminal currents at 27.6 kV-side of transformer (c) mechanical and electrical powers (d) acceleration and damping powers (e) VSG angular speed (f) power angle

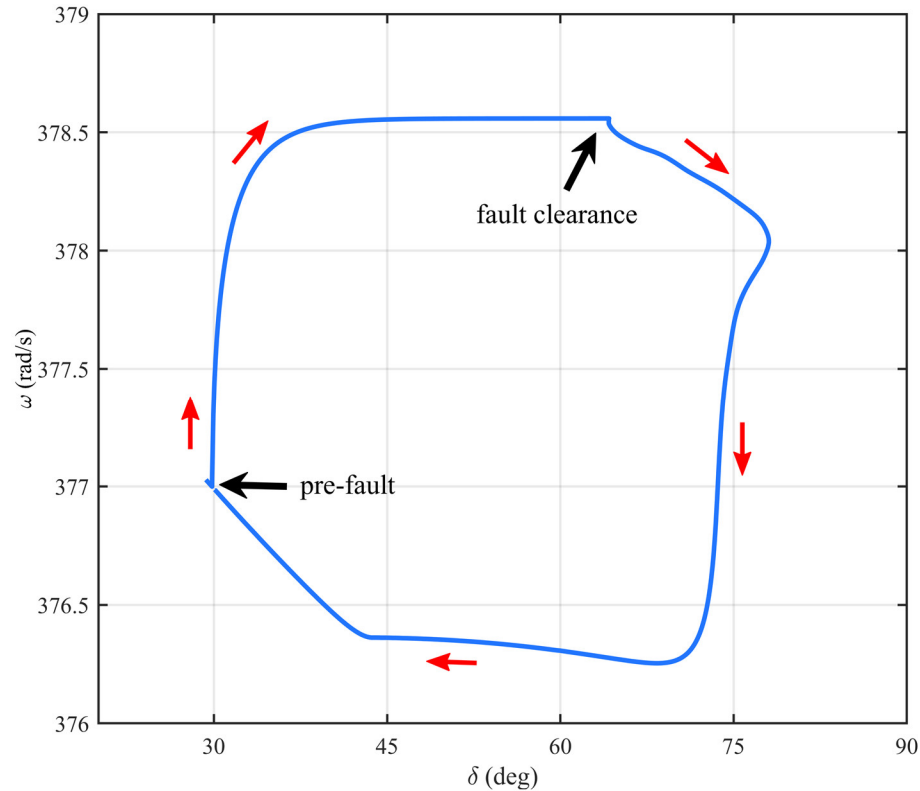


Figure 3. 8: Operating point (state transition) trajectory of the VSG with large damping, subjected to a three-phase fault

As shown in Figure 3.7, during the fault, since the output power of the VSG is zero, the VSG starts to accelerate which causes the δ and ω to increase. However, due to the large damping in VSG, the acceleration stops in around 100 ms. Once the fault is cleared at $t = 1$ s, the obtained results show that the VSG starts to decelerate and returns to its previous equilibrium.

Figure 3.8 shows the $\omega - \delta$ trajectory of the VSG with large damping factor under aforementioned fault scenario. As shown in Figure 3.8, once the fault is cleared, the ω and δ starts decreasing and the VSG starts decelerating and returns to its previous equilibrium and maintains synchronism with the grid.

It is worth mentioning that the VSG with large damping factor will not only stop the acceleration during the fault, but also help the VSG to damp the acceleration after fault clearance and maintain the VSG synchronism with the grid. However, as demonstrated by

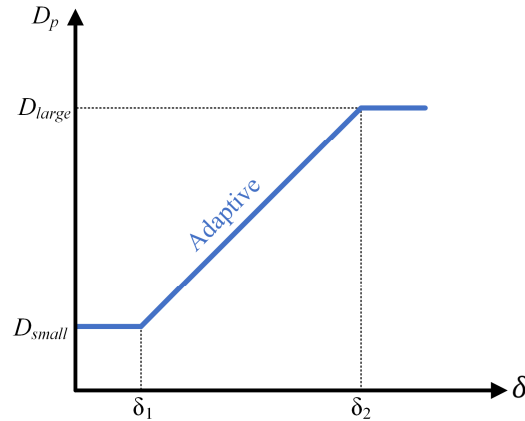


Figure 3. 9: adaptive damping characteristics

the eigenvalue analysis in the Chapter 2, a large damping results in slower response, i.e., poor dynamic behavior, of the VSG.

3.4 Proposed Adaptive Damping Strategy

In order to take advantage of the stabilizing effects of the large damping factor during and after faults, and to keep the desirable dynamics of the VSG under smaller disturbances, a simple and yet highly effective adaptive damping strategy is proposed in this section. In this method, the damping factor is a function of delta, when $\omega > 1 p.u.$ Under normal conditions, a small damping factor, i.e., the value determined using the eigenvalue analysis, is utilized. Once the virtual power angle delta exceeds a specific value δ_1 (abnormal conditions), the damping factor automatically starts to increase, depending on the value of delta. However, if $\omega < 1 p.u.$, there is no need for large damping and the adaptive damping is disabled.

Figure 3.9 shows the variations of the proposed adaptive damping with respect to the VSG angle. The proposed scheme utilizes an adaptive damping (D_p) that depends on the VSG angle (δ), as follows.

$$D_p = \begin{cases} D_{small} & , \quad \delta < \delta_1 \\ D_{small} + \frac{D_{large} + D_{small}}{\delta_2 - \delta_1} (\delta - \delta_1) & , \quad \delta_1 < \delta < \delta_2 \\ D_{large} & , \quad \delta > \delta_2 \end{cases} \quad (3.8)$$

To validate the abovementioned strategy, the performance of the VSG using adaptive damping strategy is investigated under the fault scenario of Figure 3.2. A three-phase-to-ground fault with zero resistance takes place at the same location as VSG (node N1 in Figure 3.2). To prevent unnecessary change of the damping under small disturbances, the lower input threshold is chosen as $\delta_1 = 40^\circ$. The higher input threshold is chosen as $\delta_2 = 60^\circ$.

Figure 3.10 illustrates the performance of the VSG in this case study. As shown in Figure 3.10, before the disturbance is applied at $t = 0.5$ s, the system is in steady-state, and the VSG is at the equilibrium $\delta = 30^\circ$ and $\omega = 377$ rad/s. The fault duration is 500 ms.

During the fault, since the output power of the VSG is zero, the VSG starts to accelerate which causes the δ and ω to increase. However, due to the adaptive damping scheme in VSG, the acceleration stops in around 300 ms. Once the fault is cleared at $t = 1$ s, the obtained results show that the VSG starts to decelerate and return to its previous equilibrium. Compared to the large damping strategy (Figure 3.7), the VSG returns to the pre-fault equilibrium faster.

Figure 3.11 shows the $\omega - \delta$ trajectory of the VSG with adaptive damping under aforementioned fault scenario. As shown in Figure 3.11, once the fault is cleared, the ω starts decreasing, whereas the δ jumps to around 90° and then starts falling. Thus, the VSG starts decelerating and returns to its previous equilibrium point and maintains synchronism with the grid.

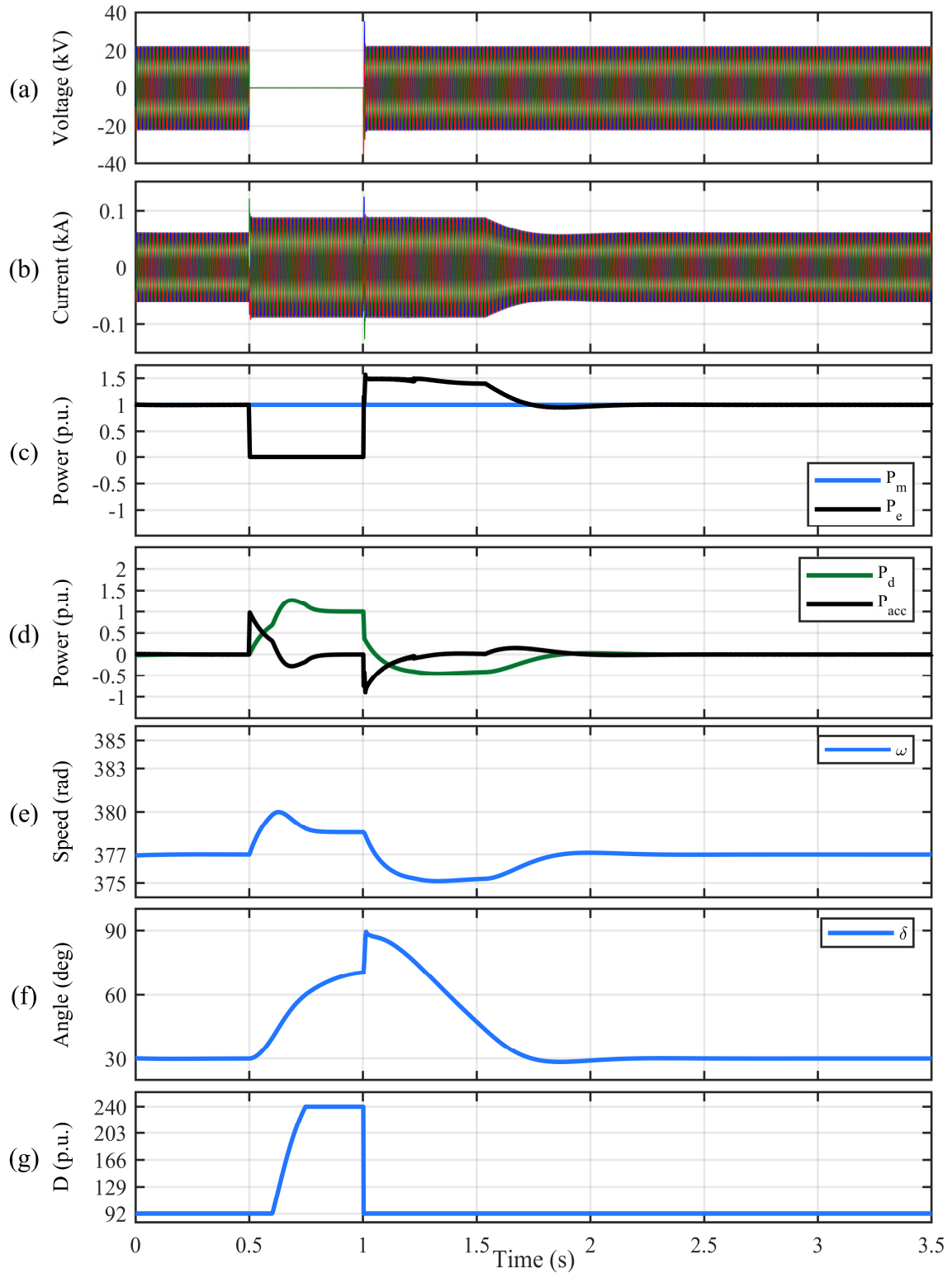


Figure 3. 10: Performance of the VSG with adaptive damping factor under a three-phase fault (a) VSG terminal voltages (at 27.6kV-side of transformer) (b) VSG terminal currents (at 27.6kV-side of transformer) (c) mechanical and electrical powers (d) acceleration and damping powers (e) VSG angular speed (f) power angle

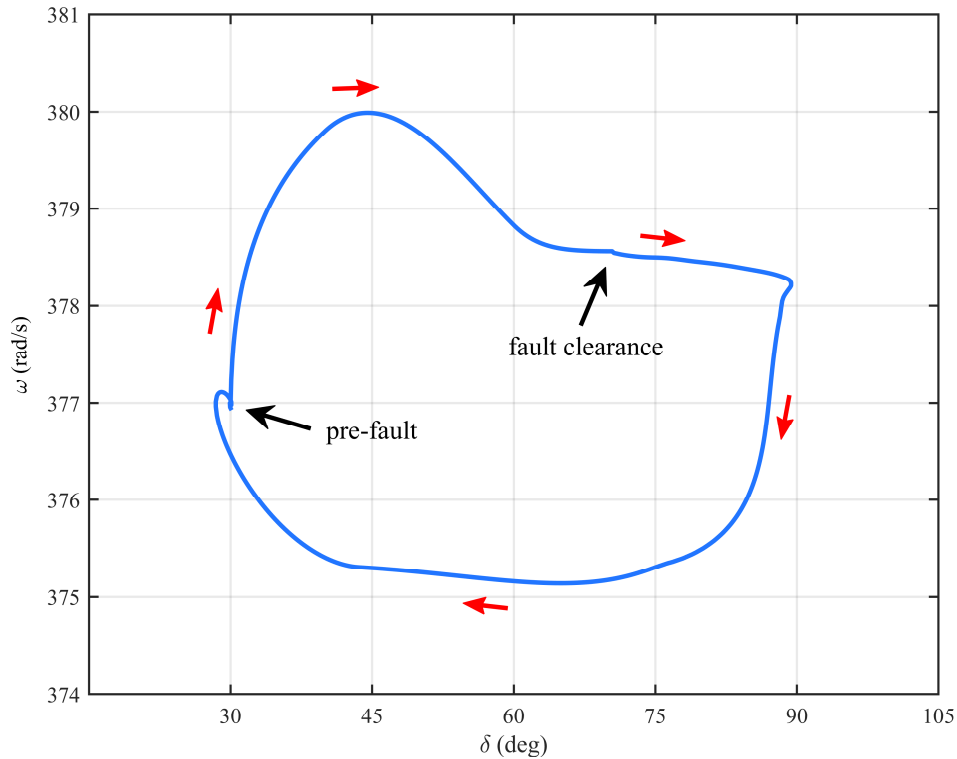


Figure 3. 11: The operating point trajectory of VSG with adaptive damping subjected to a three-phase fault

Figure 3.12 compares the operating point trajectory of VSG with different damping values, subjected to a three-phase fault. As shown in Figure 3.12, once the fault occurs, the VSG with no damping starts accelerating and never returns to the pre-fault equilibrium. However, once the fault is cleared, the other three strategies become stable.

After fault clearance, the VSG with small damping, becomes temporarily unstable and eventually reaches a new equilibrium. Although both large damping and adaptive damping maintain stable operation once the fault is cleared and return to their previous equilibrium, the adaptive damping strategy caused the VSG to reach steady-state faster than the large damping strategy. Although it looks like that the adaptive damping strategy (black curve) is going through a longer path, it reaches the equilibrium faster because of the variations of the frequency which means that the frequency drops more, so it decelerates faster.

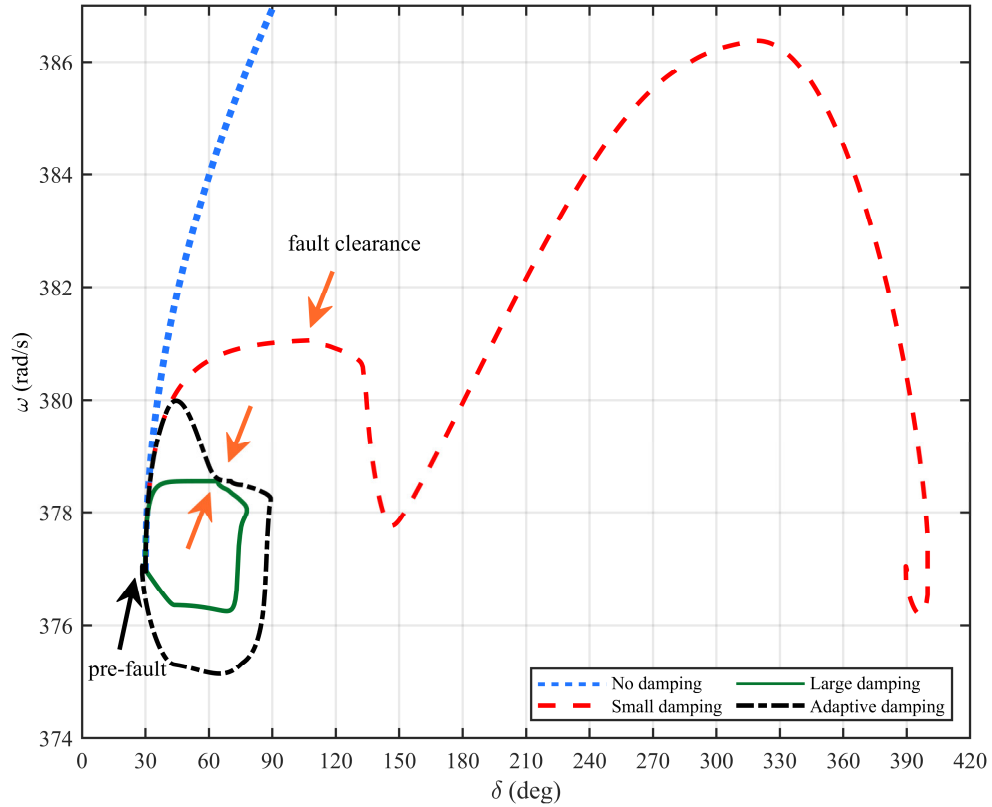


Figure 3. 12: Operating point trajectory of the VSG with different damping values

3.5 Conclusion

This chapter investigates the impacts of damping on the transient stability of the VSG. An adaptive damping strategy is proposed to improve the transient stability of the VSG and increase the CCT. The effectiveness of the proposed method is verified through time-domain simulation studies in PSCAD using a realistic study system. The study results indicate that the proposed adaptive damping strategy enables the VSG to reach steady-state in a shorter time period after fault clearance, as compared with the VSG with fixed damping values.

Chapter 4

4 Summary and Conclusions

4.1 Summary

The large-scale utilization of DERs causes a significant decrease of inertia which brings considerable concerns about grid stability. The main objective of this thesis is to develop a virtual inertia control scheme and damping strategy to improve transient stability and enable the VSG to ride through faults.

Chapter 1 presents background information on the AC microgrid, the thesis objectives, literature review and the study system. In Chapter 2, the impacts of current limiting on the transient stability of the VSG is investigated. Chapter 3 investigates the impacts of damping on transient stability of VSG. An adaptive damping strategy is proposed that are automatically adjusted depending on the VSG angle. In Chapter 4, a summary of the thesis contributions and concluding remarks are provided.

4.2 Conclusion

The conclusions drawn from this thesis are aligned with the objectives of the research to develop an adaptive virtual inertia control scheme to improve the transient stability of the VSG and enable it to ride through faults in the inverter-dominated power systems. The conclusions are as follows:

The different current limiting strategies have different impacts on the VSG output power because they lead to different values of i_d and i_q in the saturated mode. As a result, current limiting strategies affects the $P - \delta$ characteristic of the VSG and its transient stability margins. The study results indicate that although the angle priority improves the transient stability of the VSG compared to d -axis priority to a greater extent, the q -axis priority brings even more stability to the VSG. The q -axis priority current limiting strategy: (i) is identified as the most suitable current limiting strategy for improved transient stability, (ii) effectively limits overcurrent stresses under large disturbances, (iii) increases the CCT of the VSG subjected to faults (iv) enables VSG to ride through faults.

In a VSG, the virtual damping limits the increase in rotor speed and delays instability under fault condition. If the damping factor is large, the acceleration will be damped very fast, whereas if the damping factor is small, the VSG will accelerate and the acceleration will be stopped slowly. Thus, the VSG remains stable. The duration of acceleration has an inverse relation with the damping. Although the small damping limits the rotor acceleration, the VSG can become temporarily unstable under large disturbances and eventually reaches a new equilibrium. Regardless of the fault duration, the VSG with large damping factor will not only stop the acceleration during the fault, but also help the VSG to limit the acceleration after fault clearance and maintain the VSG synchronism with the grid. Therefore, to take advantage of the stabilizing effects of the large damping factor during faults, and to keep the desirable dynamics of the VSG under smaller disturbances, a simple and yet highly effective adaptive damping strategy proposed. The proposed adaptive damping strategy: (i) enables the VSG to ride through prolonged faults without becoming unstable, (ii) effectively damps the VSG acceleration under large disturbances and enhances the transient stability of VSG, (iii) improves the VSG dynamic behavior through continuous adjustment of damping, (iv) enables the VSG to recover faster after large disturbances.

The acceptable performance of the proposed adaptive damping control strategy is verified using numerous fault studies conducted on a realistic study system in the PSCAD/EMTDC software environment.

4.3 Future Work

The study results presented in this thesis provide a platform for future work on transient stability of the VSG using adaptive control. The expected future work that can complement this research includes hardware implementation of the proposed control and different current limiting strategies testing them in a real AC microgrid platform. Developing effective strategies for coordinated control of DERs in a AC microgrid is considered as future works.

References

- [1] Q. Zhong, "Virtual Inertia, Virtual Damping, and Fault Ride-through," in *Power Electronics-Enabled Autonomous Power Systems*, Wiley, 2020, pp. 203–226.
- [2] J. Fang, H. Li, Y. Tang, and F. Blaabjerg, "Distributed Power System Virtual Inertia Implemented by Grid-Connected Power Converters," *IEEE Trans. Power Electron.*, vol. 33, no. 10, pp. 8488–8499, 2018.
- [3] Q. Peng, Q. Jiang, Y. Yang, T. Liu, H. Wang, and F. Blaabjerg, "On the Stability of Power Electronics-Dominated Systems: Challenges and Potential Solutions," *IEEE Trans. Ind. Appl.*, vol. 55, no. 6, pp. 7657–7670, 2019.
- [4] P. Kundur, "Power System Stability and Control.," *New York: McGraw-Hill*, 1994. .
- [5] Q. C. Zhong and G. Weiss, "Synchronverters: Inverters that mimic synchronous generators," *IEEE Trans. Ind. Electron.*, vol. 58, no. 4, pp. 1259–1267, 2011.
- [6] H. Wu *et al.*, "Small-Signal Modeling and Parameters Design for Virtual Synchronous Generators," *IEEE Trans. Ind. Electron.*, vol. 63, no. 7, pp. 4292–4303, 2016.
- [7] J. Liu, Y. Miura, and T. Ise, "Comparison of Dynamic Characteristics between Virtual Synchronous Generator and Droop Control in Inverter-Based Distributed Generators," *IEEE Trans. Power Electron.*, vol. 31, no. 5, pp. 3600–3611, 2016.
- [8] S. D'Arco and J. A. Suul, "Equivalence of virtual synchronous machines and frequency-droops for converter-based Microgrids," *IEEE Trans. Smart Grid*, vol. 5, no. 1, pp. 394–395, 2014.
- [9] Y. Hirase, K. Sugimoto, K. Sakimoto, and T. Ise, "Analysis of Resonance in Microgrids and Effects of System Frequency Stabilization Using a Virtual Synchronous Generator," *IEEE J. Emerg. Sel. Top. Power Electron.*, vol. 4, no. 4, pp. 1287–1298, 2016.
- [10] J. Driesen and K. Visscher, "Virtual synchronous generators," in *IEEE Power and Energy Society 2008 General Meeting: Conversion and Delivery of Electrical Energy in the 21st Century, PES*, 2008.
- [11] M. A. Torres L., L. A. C. Lopes, L. A. Morán T., and J. R. Espinoza C., "Self-tuning virtual synchronous machine: A control strategy for energy storage systems to support dynamic frequency control," *IEEE Trans. Energy Convers.*, vol. 29, no. 4, pp. 833–840, 2014.
- [12] D. Li, Q. Zhu, S. Lin, and X. Y. Bian, "A Self-Adaptive Inertia and Damping Combination Control of VSG to Support Frequency Stability," *IEEE Trans. Energy Convers.*, vol. 32, no. 1, pp. 397–398, 2017.
- [13] J. Alipoor, Y. Miura, and T. Ise, "Power system stabilization using virtual synchronous generator with alternating moment of inertia," *IEEE J. Emerg. Sel. Top. Power Electron.*, vol. 3, no. 2, pp. 451–458, 2015.
- [14] N. Soni, S. Doolla, and M. C. Chandorkar, "Inertia Design Methods for Islanded Microgrids Having Static and Rotating Energy Sources," *IEEE Trans. Ind. Appl.*, vol. 52, no. 6, pp. 5165–5174, 2016.
- [15] L. Xiong *et al.*, "Static Synchronous Generator Model: A New Perspective to Investigate Dynamic Characteristics and Stability Issues of Grid-Tied PWM Inverter," *IEEE Transactions on Power Electronics*, vol. 31, no. 9. Institute of Electrical and Electronics Engineers Inc., pp. 6264–6280, 01-Sep-2016.
- [16] J. Liu, Y. Miura, H. Bevrani, and T. Ise, "Enhanced Virtual Synchronous Generator Control for Parallel Inverters in Microgrids," *IEEE Trans. Smart Grid*, vol. 8, no. 5, pp. 2268–2277, Sep. 2017.
- [17] T. Shintai, Y. Miura, and T. Ise, "Oscillation damping of a distributed generator using a virtual synchronous generator," *IEEE Trans. Power Deliv.*, vol. 29, no. 2, pp. 668–676, 2014.
- [18] S. M. Lukic, J. Cao, R. C. Bansal, F. Rodriguez, and A. Emadi, "Energy storage systems for automotive applications," *IEEE Transactions on Industrial Electronics*, vol. 55, no. 6. pp. 2258–

2267, 2008.

- [19] A. Khaligh and Z. Li, "Battery, ultracapacitor, fuel cell, and hybrid energy storage systems for electric, hybrid electric, fuel cell, and plug-in hybrid electric vehicles: State of the art," *IEEE Trans. Veh. Technol.*, vol. 59, no. 6, pp. 2806–2814, Jul. 2010.
- [20] J. Cao and A. Emadi, "A new battery/ultracapacitor hybrid energy storage system for electric, hybrid, and plug-in hybrid electric vehicles," *IEEE Trans. Power Electron.*, vol. 27, no. 1, pp. 122–132, 2012.
- [21] H. Bevrani, T. Ise, and Y. Miura, "Virtual synchronous generators: A survey and new perspectives," *Int. J. Electr. Power Energy Syst.*, vol. 54, pp. 244–254, Jan. 2014.
- [22] J. Fang, H. Li, Y. Tang, and F. Blaabjerg, "On the Inertia of Future More-Electronics Power Systems," *IEEE J. Emerg. Sel. Top. Power Electron.*, vol. 7, no. 4, pp. 2130–2146, 2019.
- [23] H. Wang and F. Blaabjerg, "Reliability of capacitors for DC-link applications in power electronic converters - An overview," in *IEEE Transactions on Industry Applications*, 2014, vol. 50, no. 5, pp. 3569–3578.
- [24] J. Fang, H. Li, and Y. Tang, "A Magnetic Integrated LLCL Filter for Grid-Connected Voltage-Source Converters," *IEEE Trans. Power Electron.*, vol. 32, no. 3, pp. 1725–1730, Mar. 2017.
- [25] Y. Huang, X. Yuan, J. Hu, P. Zhou, and D. Wang, "DC-Bus Voltage Control Stability Affected by AC-Bus Voltage Control in VSCs Connected to Weak AC Grids," *IEEE J. Emerg. Sel. Top. Power Electron.*, vol. 4, no. 2, pp. 445–457, Jun. 2016.
- [26] Y. Huang, X. Zhai, J. Hu, D. Liu, and C. Lin, "Modeling and stability analysis of VSC internal voltage in DC-link voltage control timescale," *IEEE J. Emerg. Sel. Top. Power Electron.*, vol. 6, no. 1, pp. 16–28, Mar. 2018.
- [27] L. Huang *et al.*, "A Virtual Synchronous Control for Voltage-Source Converters Utilizing Dynamics of DC-Link Capacitor to Realize Self-Synchronization," *IEEE J. Emerg. Sel. Top. Power Electron.*, vol. 5, no. 4, pp. 1565–1577, 2017.
- [28] J. Zhao, X. Lyu, Y. Fu, X. Hu, and F. Li, "Coordinated Microgrid Frequency Regulation Based on DFIG Variable Coefficient Using Virtual Inertia and Primary Frequency Control," *IEEE Trans. Energy Convers.*, vol. 31, no. 3, pp. 833–845, 2016.
- [29] J. Ekanayake and N. Jenkins, "Comparison of the response of doubly fed and fixed-speed induction generator wind turbines to changes in network frequency," *IEEE Trans. Energy Convers.*, vol. 19, no. 4, pp. 800–802, Dec. 2004.
- [30] J. Morren, S. W. H. De Haan, and J. A. Ferreira, "Contribution of DG units to primary frequency control," in *2005 International Conference on Future Power Systems*, 2005, vol. 2005.
- [31] M. F. M. Arani and E. F. El-Saadany, "Implementing virtual inertia in DFIG-based wind power generation," *IEEE Trans. Power Syst.*, vol. 28, no. 2, pp. 1373–1384, 2013.
- [32] J. Hu, H. Yuan, and X. Yuan, "Modeling of DFIG-Based WTs for Small-Signal Stability Analysis in DVC Timescale in Power Electronized Power Systems," *IEEE Trans. Energy Convers.*, vol. 32, no. 3, pp. 1151–1165, Sep. 2017.
- [33] J. Ying, X. Yuan, J. Hu, and W. He, "Impact of Inertia Control of DFIG-Based WT on Electromechanical Oscillation Damping of SG," *IEEE Trans. Power Syst.*, vol. 33, no. 3, pp. 3450–3459, May 2018.
- [34] J. Fang, H. Li, Y. Tang, and F. Blaabjerg, "On the Inertia of Future More-Electronics Power Systems," *IEEE J. Emerg. Sel. Top. Power Electron.*, vol. 7, no. 4, pp. 2130–2146, 2019.
- [35] W. S. Im, C. Wang, W. Liu, L. Liu, and J. M. Kim, "Distributed virtual inertia based control of multiple photovoltaic systems in autonomous microgrid," *IEEE/CAA J. Autom. Sin.*, vol. 4, no. 3, pp. 512–519, Jul. 2017.

- [36] N. Kakimoto, S. Takayama, H. Satoh, and K. Nakamura, "Power modulation of photovoltaic generator for frequency control of power system," *IEEE Trans. Energy Convers.*, vol. 24, no. 4, pp. 943–949, Dec. 2009.
- [37] X. Lyu, X. Zhao, J. Zhao, and K. P. Wong, "Advanced frequency support strategy of photovoltaic system considering changing working conditions," *IET Gener. Transm. Distrib.*, vol. 12, no. 2, pp. 363–370, Jan. 2018.
- [38] J. Jongudomkarn, J. Liu, and T. Ise, "Virtual Synchronous Generator Control with reliable Fault Ride-Through ability: A solution based on Finite-Set Model Predictive Control," *IEEE J. Emerg. Sel. Top. Power Electron.*, vol. 6777, no. c, pp. 1–1, 2019.
- [39] M. Choopani, S. H. Hosseinian, and B. Vahidi, "New Transient Stability and LVRT Improvement of Multi-VSG Grids Using the Frequency of the Center of Inertia," *IEEE Trans. Power Syst.*, vol. 35, no. 1, pp. 527–538, 2020.
- [40] J. Daalder and D. Karlsson, "Grid Codes Comparison," Göteborg, Sweden, 2006.
- [41] A. D. Paquette and D. M. Divan, "Virtual Impedance Current Limiting for Inverters in Microgrids With Synchronous Generators," *IEEE Trans. Ind. Appl.*, vol. 51, no. 2, pp. 1630–1638, 2015.
- [42] "THE GRID CODE ISSUE 5," 2017.
- [43] "IEEE Standard for Interconnection and Interoperability of Distributed Energy Resources with Associated Electric Power Systems Interfaces," *IEEE Std 1547-2018 (Revision of IEEE Std 1547-2003)*. pp. 1–138, 2018.
- [44] T. Qoria, F. Gruson, F. Colas, G. Denis, T. Prevost, and X. Guillaud, "Critical clearing time determination and enhancement of grid-forming converters embedding virtual impedance as current limitation algorithm," *IEEE J. Emerg. Sel. Top. Power Electron.*, vol. 8, no. 2, pp. 1–1, 2019.
- [45] H. R. Baghaee, M. Mirsalim, G. B. Gharehpetian, and H. A. Talebi, "A Decentralized Robust Mixed H₂/H_∞ Voltage control scheme to improve small/large-signal stability and FRT capability of islanded multi-der microgrid considering load disturbances," *IEEE Syst. J.*, vol. 12, no. 3, pp. 2610–2621, Sep. 2018.
- [46] J. Liu, D. Yang, W. Yao, R. Fang, H. Zhao, and B. Wang, "PV-based virtual synchronous generator with variable inertia to enhance power system transient stability utilizing the energy storage system," *Prot. Control Mod. Power Syst.*, vol. 2, no. 1, p. 39, Dec. 2017.
- [47] Y. Cao *et al.*, "A Virtual Synchronous Generator Control Strategy for VSC-MTDC Systems," *IEEE Trans. Energy Convers.*, vol. 33, no. 2, pp. 750–761, 2018.
- [48] B. Li and L. Zhou, "Power Decoupling Method Based on the Diagonal Compensating Matrix for VSG-Controlled Parallel Inverters in the Microgrid," *Energies*, vol. 10, no. 12, p. 2159, Dec. 2017.
- [49] K. Shi, G. Zhou, P. Xu, H. Ye, and F. Tan, "The Integrated Switching Control Strategy for Grid-Connected and Islanding Operation of Micro-Grid Inverters Based on a Virtual Synchronous Generator," *Energies*, vol. 11, no. 6, pp. 1–20, 2018.
- [50] K. Shi, W. Song, H. Ge, P. Xu, Y. Yang, and F. Blaabjerg, "Transient Analysis of Microgrids with Parallel Synchronous Generators and Virtual Synchronous Generators," *IEEE Trans. Energy Convers.*, vol. PP, no. c, pp. 1–1, 2019.
- [51] L. Huang, H. Xin, Z. Wang, L. Zhang, K. Wu, and J. Hu, "Transient Stability Analysis and Control Design of Droop-Controlled Voltage Source Converters Considering Current Limitation," *IEEE Trans. Smart Grid*, vol. 10, no. 1, pp. 578–591, 2019.
- [52] H. Xin, L. Huang, L. Zhang, Z. Wang, and J. Hu, "Synchronous Instability Mechanism of P-f Droop-Controlled Voltage Source Converter Caused by Current Saturation," *IEEE Trans. Power Syst.*, vol. 31, no. 6, pp. 5206–5207, 2016.
- [53] L. Huang, L. Zhang, H. Xin, Z. Wang, and D. Gan, "Current limiting leads to virtual power angle synchronous instability of droop-controlled converters," *IEEE Power Energy Soc. Gen. Meet.*, vol.

- 2016-Novem, no. 201, pp. 1–5, 2016.
- [54] M. Ebrahimi, S. A. Khajehoddin, and M. Karimi-Ghartemani, “An Improved Damping Method for Virtual Synchronous Machines,” *IEEE Trans. Sustain. Energy*, vol. 10, no. 3, pp. 1491–1500, 2019.
- [55] “COMMISSION REGULATION (EU) 2016/ 631 - of 14 April 2016 - establishing a network code on requirements for grid connection of generators.”
- [56] J. Alipoor, Y. Miura, and T. Ise, “Stability assessment and optimization methods for microgrid with multiple VSG units,” *IEEE Trans. Smart Grid*, vol. 9, no. 2, pp. 1462–1471, 2018.
- [57] K. Wang, C. Qi, X. Huang, and G. Li, “Large disturbance stability evaluation of interconnected multi-inverter power grids with VSG model,” *J. Eng.*, vol. 2017, no. 13, pp. 2483–2488, 2017.
- [58] G. Denis, T. Prevost, M. S. Debry, F. Xavier, X. Guillaud, and A. Menze, “The migrate project: The challenges of operating a transmission grid with only inverter-based generation. A grid-forming control improvement with transient current-limiting control,” *IET Renew. Power Gener.*, vol. 12, no. 5, pp. 523–529, 2018.
- [59] Z. Shuai, C. Shen, X. Liu, Z. Li, and Z. John Shen, “Transient angle stability of virtual synchronous generators using lyapunov’s direct method,” *IEEE Trans. Smart Grid*, vol. 10, no. 4, pp. 4648–4661, 2019.
- [60] X. Yang and H. Chen, “Characteristics and restraining strategy of fault current in VSG,” *Electron. Lett.*, vol. 55, no. 20, pp. 1104–1106, 2019.
- [61] M. Yu, W. Huang, N. Tai, X. Zheng, P. Wu, and W. Chen, “Transient stability mechanism of grid-connected inverter-interfaced distributed generators using droop control strategy,” *Appl. Energy*, vol. 210, pp. 737–747, Jan. 2018.
- [62] H. Cheng, Z. Shuai, C. Shen, X. Liu, Z. Li, and Z. J. Shen, “Transient Angle Stability of Paralleled Synchronous and Virtual Synchronous Generators in Islanded Microgrids,” *IEEE Trans. Power Electron.*, vol. 8993, no. c, pp. 1–1, 2020.
- [63] Denis Guillaume, “From grid-following to grid-forming: The new strategy to build 100 % power-electronics interfaced transmission system with enhanced transient behavior.,” *PhD Thesis*, Nov-2017.
- [64] E. Hammad, A. Farraj, and D. Kundur, “On Effective Virtual Inertia of Storage-Based Distributed Control for Transient Stability,” *IEEE Trans. Smart Grid*, vol. 10, no. 1, pp. 327–336, 2019.
- [65] X. Lu, J. Wang, J. M. Guerrero, and D. Zhao, “Virtual-impedance-based fault current limiters for inverter dominated AC microgrids,” *IEEE Trans. Smart Grid*, vol. 9, no. 3, pp. 1599–1612, May 2018.
- [66] F. Salha, F. Colas, and X. Guillaud, “Virtual resistance principle for the overcurrent protection of PWM voltage source inverter,” *IEEE PES Innov. Smart Grid Technol. Conf. Eur. ISGT Eur.*, pp. 1–6, 2010.
- [67] J. Jongudomkarn, J. Liu, and T. Ise, “Comparison of Current-Limiting Strategies of Virtual Synchronous Generator Control during Fault Ride-Through,” *IFAC-PapersOnLine*, vol. 51, no. 28, pp. 256–261, Jan. 2018.
- [68] T. Zheng, L. Chen, Y. Guo, and S. Mei, “Comprehensive control strategy of virtual synchronous generator under unbalanced voltage conditions,” *IET Gener. Transm. Distrib.*, vol. 12, no. 7, pp. 1621–1630, 2018.
- [69] Y. Yu and X. Hu, “Active Disturbance Rejection Control Strategy for Grid-Connected Photovoltaic Inverter Based on Virtual Synchronous Generator,” *IEEE Access*, vol. 7, pp. 17328–17336, 2019.
- [70] S. D’Arco, J. A. Suul, and O. B. Fosso, “Small-signal modeling and parametric sensitivity of a virtual synchronous machine in islanded operation,” *Int. J. Electr. Power Energy Syst.*, vol. 72, pp. 3–15, 2015.

- [71] T. K. Abdel-Galil Ahmed EB Abu-Elanien, E. F. Ehab El-Saadany Adly Girgis Yasser A-R I Mohamed, and E. M. Magdy A Salama Hatem H M Zeineldin, "PROTECTED BUSINESS INFORMATION PROTECTION COORDINATION PLANNING WITH DISTRIBUTED GENERATION," 2007.
- [72] B. Li, L. Zhou, X. Yu, C. Zheng, and J. Liu, "Improved power decoupling control strategy based on virtual synchronous generator," *IET Power Electron.*, vol. 10, no. 4, pp. 462–470, 2017.
- [73] K. Shi, W. Song, P. Xu, R. Liu, Z. Fang, and Y. Ji, "Low-Voltage Ride-Through Control Strategy for a Virtual Synchronous Generator Based on Smooth Switching," *IEEE Access*, vol. 6, pp. 2703–2711, 2017.
- [74] S. A. Khajehoddin, M. Karimi-Ghartemani, and M. Ebrahimi, "Grid-supporting inverters with improved dynamics," *IEEE Trans. Ind. Electron.*, vol. 66, no. 5, pp. 3655–3667, 2019.
- [75] H. Zhao, Q. Yang, and H. Zeng, "Multi-loop virtual synchronous generator control of inverter-based DGs under microgrid dynamics," *IET Gener. Transm. Distrib.*, vol. 11, no. 3, pp. 795–803, 2017.
- [76] S. Y. Altahir, X. Yan, and A. S. Gadalla, "Active and reactive power sharing control strategy for VSGs in microgrid considering the different capacities of distributed energy resources," *IET Cyber-Physical Syst. Theory Appl.*, vol. 3, no. 3, pp. 167–173, 2018.
- [77] X. Yan, S. Y. A. Mohamed, D. Li, and A. S. Gadalla, "Parallel operation of virtual synchronous generators and synchronous generators in a microgrid," *J. Eng.*, vol. 2019, no. 16, pp. 2635–2642, 2019.
- [78] Q. C. Zhong, P. L. Nguyen, Z. Ma, and W. Sheng, "Self-synchronized synchronverters: Inverters without a dedicated synchronization unit," *IEEE Trans. Power Electron.*, vol. 29, no. 2, pp. 617–630, 2014.
- [79] K. Shi, H. Ye, P. Xu, D. Zhao, and L. Jiao, "Low-voltage ride through control strategy of virtual synchronous generator based on the analysis of excitation state," *IET Gener. Transm. Distrib.*, vol. 12, no. 9, pp. 2165–2172, 2018.
- [80] M. Ashabani and Y. A. R. I. Mohamed, "Integrating VSCs to weak grids by nonlinear power damping controller with self-synchronization capability," *IEEE Trans. Power Syst.*, vol. 29, no. 2, pp. 805–814, 2014.
- [81] F. Wang, L. Zhang, X. Feng, and H. Guo, "An Adaptive Control Strategy for Virtual Synchronous Generator," *IEEE Trans. Ind. Appl.*, vol. 54, no. 5, pp. 5124–5133, 2018.
- [82] Y. Wang, B. Liu, and S. Duan, "Modified virtual inertia control method of VSG strategy with improved transient response and power-supporting capability," *IET Power Electron.*, vol. 12, no. 12, pp. 3178–3184, 2019.
- [83] X. Meng, J. Liu, and Z. Liu, "A Generalized Droop Control for Grid-Supporting Inverter Based on Comparison between Traditional Droop Control and Virtual Synchronous Generator Control," *IEEE Trans. Power Electron.*, vol. 34, no. 6, pp. 5416–5438, 2019.
- [84] W. Yan, L. Cheng, S. Yan, W. Gao, and W. Gao, "Enabling and Evaluation of Inertial Control for PMSG-WTG using Synchronverter with Multiple Virtual Rotating Masses in Microgrid," *IEEE Trans. Sustain. Energy*, vol. PP, no. c, pp. 1–1, 2019.
- [85] A. Fernández-Guillamón, A. Viguera-Rodríguez, and Á. Molina-García, "Analysis of power system inertia estimation in high wind power plant integration scenarios," *IET Renew. Power Gener.*, vol. 13, no. 15, pp. 2807–2816, 2019.
- [86] V. Natarajan and G. Weiss, "Synchronverters with Better Stability Due to Virtual Inductors, Virtual Capacitors, and Anti-Windup," *IEEE Trans. Ind. Electron.*, vol. 64, no. 7, pp. 5994–6004, 2017.
- [87] A. Karimi *et al.*, "Inertia Response Improvement in AC Microgrids: A Fuzzy-Based Virtual Synchronous Generator Control," *IEEE Trans. Power Electron.*, vol. 35, no. 4, pp. 4321–4331, 2020.
- [88] O. Mo, S. Darco, and J. A. Suul, "Evaluation of Virtual Synchronous Machines with Dynamic or

- Quasi-Stationary Machine Models,” *IEEE Trans. Ind. Electron.*, vol. 64, no. 7, pp. 5952–5962, 2017.
- [89] J. Liu, Y. Miura, and T. Ise, “Fixed-Parameter Damping Methods of Virtual Synchronous Generator Control Using State Feedback,” *IEEE Access*, vol. 7, pp. 99177–99190, 2019.
- [90] L. Huang, H. Xin, and Z. Wang, “Damping Low-Frequency Oscillations Through VSC-HVdc Stations Operated as Virtual Synchronous Machines,” *IEEE Trans. Power Electron.*, vol. 34, no. 6, pp. 5803–5818, 2019.
- [91] L. Xu, H. Xin, L. Huang, H. Yuan, P. Ju, and D. Wu, “Symmetric Admittance Modeling for Stability Analysis of Grid-Connected Converters,” *IEEE Trans. Energy Convers.*, vol. 35, no. 1, pp. 434–444, 2020.
- [92] F. Milano and Á. O. Manjavacas, *Converter-Interfaced Energy Storage Systems*. Cambridge University Press, 2019.
- [93] M. G. Taul, X. Wang, P. Davari, and F. Blaabjerg, “Current Limiting Control with Enhanced Dynamics of Grid-Forming Converters during Fault Conditions,” *IEEE J. Emerg. Sel. Top. Power Electron.*, vol. 8, no. 2, pp. 1–1, 2019.
- [94] A. Tayyebi, D. Groß, A. Anta, F. Kupzog, and F. Dörfler, “Interactions of Grid-Forming Power Converters and Synchronous Machines,” no. 691800, pp. 1–26, 2019.
- [95] L. Zhang, *Modeling and Control of VSC-HVDC Links Connected to Weak AC Systems*. .
- [96] M. N. Marwali and A. Keyhani, “Control of distributed generation systems - Part I: Voltages and currents control,” *IEEE Trans. Power Electron.*, vol. 19, no. 6, pp. 1541–1550, 2004.
- [97] M. A. Zamani, A. Yazdani, and T. S. Sidhu, “A control strategy for enhanced operation of inverter-based microgrids under transient disturbances and network faults,” *IEEE Trans. Power Deliv.*, vol. 27, no. 4, pp. 1737–1747, 2012.
- [98] J. W. Choi and S. K. Sul, “Fast current controller in three-phase AC/DC boost converter using d-q axis crosscoupling,” *IEEE Trans. Power Electron.*, vol. 13, no. 1, pp. 179–185, 1998.
- [99] M. Li, W. Huang, N. Tai, M. Yu, Y. Lu, and C. Ni, “Transient Behavior Analysis of VSG-IIDG during Disturbances Considering the Current Limit Unit,” *IEEE Power Energy Soc. Gen. Meet.*, vol. 2019-Augus, pp. 6–10, 2019.
- [100] X. Pei and Y. Kang, “Short-circuit fault protection strategy for high-power three-phase three-wire inverter,” *IEEE Trans. Ind. Informatics*, vol. 8, no. 3, pp. 545–553, 2012.
- [101] S. Li, L. Xu, and T. A. Haskew, “Control of VSC-based STATCOM using conventional and direct-current vector control strategies,” *Int. J. Electr. Power Energy Syst.*, vol. 45, no. 1, pp. 175–186, 2013.
- [102] Z. Bian and Z. Xu, “Fault Ride-Through Capability Enhancement Strategy for VSC-HVDC Systems Supplying for Passive Industrial Installations,” *IEEE Trans. Power Deliv.*, vol. 31, no. 4, pp. 1673–1682, 2016.
- [103] Y. Liu and Z. Chen, “A flexible power control method of VSC-HVDC link for the enhancement of effective short-circuit ratio in a hybrid multi-infeed HVDC system,” *IEEE Trans. Power Syst.*, vol. 28, no. 2, pp. 1568–1581, 2013.
- [104] C. Du, M. H. J. Bollen, E. Agneholm, and A. Sannino, “A new control strategy of a VSC-HVDC system for high-quality supply of industrial plants,” *IEEE Trans. Power Deliv.*, vol. 22, no. 4, pp. 2386–2394, 2007.
- [105] R. Ottersten and J. Svensson, “Vector current controlled voltage source converter - Deadbeat control and saturation strategies,” *IEEE Trans. Power Electron.*, vol. 17, no. 2, pp. 279–285, 2002.
- [106] M. A. A. Murad, A. Ortega, and F. Milano, “Impact on power system dynamics of PI control limiters of VSC-Based devices,” *20th Power Syst. Comput. Conf. PSCC 2018*, 2018.
- [107] and T. J. O. J. Duncan Glover, Mulukutla S. Sarma, “Power System Analysis and Design,” *Fifth*

Edition, Cengage Learning, 2008.

- [108] Ehsan Abbasi et al, "Typical Canadian medium voltage benchmark network model for integration of distributed energy resources," *CIGRE-782, Vancouver, BC, Canada, Oct-2016.*

Appendices A: Study System Parameters

Table A. 1: Study system parameters

Component	Description
Grid	$V_{LL-base} = 27.6$ kV, 60 Hz $S_{base} = 20$ MVA, SSC = 885.33, $X/R = 10$
Capacitor bank	$Q = 1.5$ MVAR
Transformers	T1: 3.6 MVA, 6% impedance 27.6 kV/8.31 kV, ΔY T2: 15 MVA, 7.3% impedance 27.6 kV/27.6 kV, YY T3: 1 MVA, 4% impedance 27.6 kV/8.31 kV, ΔY T4: 3.6 MVA, 5.65% impedance 27.6 kV/8.31 kV, ΔY
Overhead lines	Spacing ID = STD-3PH-NBP [108] $R_l = 0.172$ Ω /km, $R_0 = 0.491$ Ω /km $X_l = 0.404$ Ω /km, $X_0 = 1.354$ Ω /km $B_l = 4.171$ uS/km, $B_0 = 1.759$ uS/km

Table A. 2: Overhead line length

Line	Length (m)	Line	Length (m)	Line	Length (m)
L1	5700	L11	3330	L21	1550
L2	1010	L12	1030	L22	2120
L3	400	L13	3490	L23	1820
L4	380	L14	1430	L24	2540
L5	120	L15	190	L25	620
L6	170	L16	1940	L26	3580
L7	260	L17	2450	L27	770
L8	140	L18	1630	L28	2080
L9	940	L19	1200	L29	4510
L10	300	L20	820	L30	4040

Table A. 3: Load specification

Three Phase (kVA)	Power Factor
2364	0.95
346	0.87
3355	0.95
256	0.75
6.3	1
265	0.95
650	1
50	0.95
160	0.95
205	1
445	0.95
10	0.95
215	0.95
85	0.95
110	0.95
2280	0.95

Appendices B: VSG Output Power Characteristics

According to Figure 2.3, the VSG output current is calculated as (B.1).

$$I = |I|\angle\theta = \frac{E\angle\delta - V\angle 0}{jX_v} = \frac{E\sin\delta}{X_v} - j\left(\frac{E\cos\delta}{X_v} - \frac{V}{X_v}\right) \quad (\text{B.1})$$

$$I_{Re} = \frac{E\sin\delta}{X_v}, \quad I_{Im} = -\left(\frac{E\cos\delta}{X_v} - \frac{V}{X_v}\right) \quad (\text{B.2})$$

$$I_{mag} = \left|\frac{V\angle\delta - U\angle 0}{jX_v}\right|, \quad \theta = \frac{\delta}{2} \quad (\text{B.3})$$

According to Figure 2.10, the dq reference currents and voltages are calculated as (B.4) and (B.5), respectively.

$$i_d^{ref*} = I_{mag}\cos\frac{\delta}{2}, \quad i_q^{ref*} = I_{mag}\sin\frac{\delta}{2} \quad (\text{B.4})$$

$$v_d = V\cos\delta, \quad v_q = V\sin\delta \quad (\text{B.5})$$

By substituting equations (B.2) into (B.6), the VSG output power in unsaturated mode can be rewritten as (B.7).

$$S = VI^* = \frac{EV\sin\delta}{X} + j\left(\frac{EV\cos\delta}{X} - \frac{V^2}{X}\right) \quad (\text{B.6})$$

$$P_{um} = \frac{EV}{X}\sin\delta, \quad Q_{um} = \frac{EV}{X}\cos\delta - \frac{V^2}{X} \quad (\text{B.7})$$

Based on the different current limiting strategies, the saturated output power formulas are proven as follows:

saturated output power in angle priority: As for simplicity, assume $V=1$ p.u., $E=1$ p.u. Therefore, (B.7) will be simplified to (B.8).

$$P_{um} = \frac{1}{X}\sin\delta, \quad Q_{um} = \frac{1}{X}\cos\delta - \frac{1}{X} \quad (\text{B.8})$$

From the above equation, we can obtain the saturated mode active power output as (B.9).

$$P_{sm} = P_{um} \times \frac{I_{max}}{\sqrt{P_{um}^2 + Q_{um}^2}} \quad (\text{B.9})$$

By substituting equations (B.8) into (B.9), (B.9) can be rewritten as (B.10).

$$\begin{aligned} P_{sm} &= \frac{1}{X} \sin\delta \times \frac{I_{max}}{\sqrt{\left(\frac{1}{X} \sin\delta\right)^2 + \left(\frac{\cos\delta - 1}{X}\right)^2}} = \\ &= \frac{I_{max} \sin\delta}{\sqrt{(\sin\delta)^2 + (\cos\delta - 1)^2}} = \frac{I_{max} \sin\delta}{\sqrt{2 - 2\cos\delta}} = \\ &= \frac{I_{max} \sin\delta}{\sqrt{2 \left(2 \sin^2\left(\frac{\delta}{2}\right)\right)}} = \frac{I_{max} \sin\delta}{2 \sin\left(\frac{\delta}{2}\right)} = \\ &= \frac{I_{max} \left(2 \sin\left(\frac{\delta}{2}\right) \cos\left(\frac{\delta}{2}\right)\right)}{2 \sin\left(\frac{\delta}{2}\right)} = I_{max} \cos\frac{\delta}{2} \end{aligned} \quad (\text{B.10})$$

saturated output power in d-axis reference current priority:

Based on the d-axis current magnitude, saturated output power is calculated by either (B.11) or (B.12).

If $(i_d^{ref*} \geq I_{max})$, then $i_d^{ref} = I_{max}$ (with i_d^{ref*} sign) and $i_q^{ref} = 0$.

$$P_{out} = v_d i_d + v_q i_q = V I_{max} \cos\delta \quad (\text{B.11})$$

Otherwise:

$$\begin{aligned} P_{out} &= v_d i_d + v_q i_q = V i_d^{ref*} \cos\delta \\ &+ V \sqrt{I_{max}^2 - i_d^{ref*2}} \sin\delta \end{aligned} \quad (\text{B.12})$$

saturated output power in q-axis reference current priority:

Based on q-axis current magnitude, saturated output power is calculated by either (B.13) or (B.14).

If ($i_q^{ref*} \geq I_{max}$), then $i_q^{ref} = I_{max}, i_d^{ref} = 0$.

$$P_{out} = v_d i_d + v_q i_q = VI_{max} \sin \delta \quad (\text{B.13})$$

Otherwise:

$$P_{out} = v_d i_d + v_q i_q = V \sqrt{I_{max}^2 - i_q^{ref*2}} \cos \delta + V i_q^{ref*} \sin \delta \quad (\text{B.14})$$

Curriculum Vitae

Name:	Kourosch Gharouni Saffar
Post-Secondary Education and Degrees:	<p>Western University London, ON, Canada 2018 – 2020, M.E.Sc. in Electrical and Computer Engineering</p> <p>Ferdowsi University Mashhad, Khorasan Razavi, Iran 2013-2017, B.Sc. in Electrical Engineering</p>
Related Work Experience:	<ul style="list-style-type: none"> • Graduate Research Assistant Western University 2018 –2020 • Graduate Teaching Assistant Western University 2018 –2020